UNIVERSITY OF CALIFORNIA

Los Angeles

Formation Mechanism of Porous Cu_3Sn Intermetallic Compounds in Microbumps for 3D-IC Packaging

A dissertation submitted in partial satisfaction

of the requirements for the degree Doctor of Philosophy

in Materials Science and Engineering

by

Tawei Chu

2018

ABSTRACT OF THE DISSERTATION

Formation Mechanism of Porous Cu_3Sn Intermetallic Compounds

in Microbumps for 3D-IC Packaging

by

Tawei Chu

Doctor of Philosophy in Materials Science and Engineering

University of California, Los Angeles, 2018

Professor King-Ning Tu, Co-Chair

Professor Jenn-Ming Yang, Co-Chair

This thesis presents a study on the formation mechanism of porous Cu_3Sn intermetallic compounds in microbumps for 3D-IC packaging, which are issues of importance to the packaging technology in microelectronic industry. Experimental emphases are on the formation processes of porous Cu_3Sn under current stressing and by solid state aging. Theoretical interpretations of the observations are also presented.

Following a background introduction, we first report the results on electromigration tests of SnAg solder bump samples with 15 μm bump height and Cu under-bump-metallization (UBM). The test conditions were 1.45×10^4 A/cm^2 at 185 ^{o}C and 1.20×10^4 A/cm^2 at 0 ^{o}C. A porous Cu_3Sn intermetallic compound (IMC) structure was observed to form within the bumps after several hundred hours of current stressing. In direct comparison, annealing alone

at 185 ^{o}C will take more than 1000 h for porous Cu_3Sn to form, and it will not form at 170 ^{o}C even after 2000 h. A mechanism is proposed to explain the formation of this porous structure assisted by electromigration. The results show that the SnAg bump with low bump height will become porous-type Cu_3Sn when stressing with high current density and high temperature. Polarity effects on porous Cu_3Sn formation is also examined and interpreted.

The second part of the experimental study is on the growth competition between the co-existing layer-type and porous-type Cu_3Sn in solder microbumps of Cu/SnAg/Cu. The thickness of the SnAg solder is about 14 μm and the Cu column on both sides is 20 μm. Upon wetting-reflow, the solder is reacted completely to form Cu-Sn intermetallic compounds in a multi-layered structure of $Cu/Cu_3Sn/Cu_6Sn_5/Cu_3Sn/Cu$. Upon further annealing at 220 °C and 260 °C, we obtain Cu/Cu_3Sn/porous $Cu_3Sn/Cu_3Sn/Cu$, in which both types of Cu_3Sn co-exist and form an interface. In the layer-type growth, we assume Cu to be the dominant diffusing species, coming from the Cu column. The Cu reacts with Cu_6Sn_5 to grow the Cu_3Sn layer. In the porous-type growth, we assume Sn to be the dominant diffusing species, coming from the depletion of Sn in Cu_6Sn_5. The depleted Cu_6Sn_5 transforms to the porous-type Cu_3Sn. At the same time, the Sn diffuses to the side-wall of Cu column to form a coating of Cu_3Sn. Experimental observations of 3-dimensional distribution of voids in the porous-type Cu_3Sn are performed by synchrotron radiation tomography; the voids are interconnected for the out-diffusion of Sn. The competing growth between the layer-type and the porous-type Cu_3Sn is analyzed.

Lastly, for a theoretical understanding, we discuss the mechanism of this unique porous void formation in microbumps, including the necessary and sufficient conditions of porous Cu_3Sn formation and a comparison between incomplete and complete cellular precipitations.

The dissertation of Tawei Chu is approved.

Subramanian Iyer

Ya-Hong Xie

King-Ning Tu, Committee Co-Chair

Jenn-Ming Yang, Committee Co-Chair

University of California, Los Angeles

2018

This dissertation is dedicated to my parents.

TABLE OF CONTENTS

LIST OF FIGURES

LIST OF TABLES

ACKNOWLEDGEMENTS

Most of all, I would like to extend my heartfelt gratitude to my advisor, Professor King-Ning Tu, for his support and encouragement throughout the course of this thesis research. He has not only guided me to the frontiers of materials science, but also treated me with his characteristic kindness, generosity, and patience. I shall treasure both blessings forever.

I would also like to sincerely thank Professor Subramanian S. Iyer, Professor Ya-Hong Xie**,** and Professor Jenn-Ming Yang for kindly agreeing to serve on the dissertation committee and providing invaluable guidance in the final stage of my thesis research.

The experimental part of the thesis (Chapters 2 and 3) is mostly based on the following 2 papers (with some additional data since their publications):

1. D. T. Chu, Y.C. Chu, J. A. Lin, Y. T. Chen, C. C. Wang, Y. F. Song, C. C. Chiang, C. Chen, and K. N. Tu, Growth competition between layer-type and porous-type Cu_3Sn in microbumps. Microelectronics Reliability 79, 32-37 (2017).

2. J. A. Lin, C. K. Lin, C. M. Liu, Y. S. Huang, C. Chen, D. T. Chu, and K. N. Tu, Formation mechanism of porous Cu_3Sn intermetallic compounds by high current stressing at high temperatures in low-bump-height solder joints. Crystals 6, 12 (2016).

The experiments were carried out in collaboration with the group at National Chiao Tung University (NCTU) led by Professor Chih Chen. It has been a great privilege to work at NCTU under the guidance of Prof. Chen, to whom I am deeply grateful. Contributions from all co-authors are gratefully acknowledged. I am also indebted to the National Synchrotron Radiation Center in Taiwan for providing a world class transmission X-ray microscope and personnel support to obtain the critical data featured in the first reference listed above.

Theoretical interpretation of the experiments (Chapter 4) is based on the paper by Y. Wang, D. T. Chu, and K. N. Tu [Porous Cu_3Sn formation in Cu-Sn IMC-based micro-joints.

IEEE ECTC Proceedings, pp. 439-446 (2016)].

It is extremely rewarding to learn the deep physical insights into the results presented in this thesis from a recent paper by Professors Tu and Gusak [A comparison between complete and incomplete cellular precipitations. Scr. Materialia 146, 133–135 (2018)]. These insights are discussed in my own words in Chapter 5, together with 3 new figures (Figures 5-2, 5-3, and 5-6) to illustrate the key points of their paper.

Lastly, a passionate “thank you for everything” to my beloved parents, to whom this thesis is dedicated.

VITA

June, 2008	B.S. Department of Physics National Tsing Hua University Hsinchu, Taiwan
June, 2010	M.S. Department of Materials Science and Engineering Stanford University
Sept. 2010 – Sept. 2011	Junior Development Engineer Nanolab, UCLA Los Angeles, CA, USA
June 2013 – Jan. 2014	Process Engineering Internship Intel Corporation Chandler, AZ, USA
Sept. 2014 – Feb. 2015	Reliability Engineering Internship Intel Corporation Chandler, AZ, USA
Sept. 2018	PhD (expected) Department of Materials Science and Engineering University of California, Los Angeles Los Angeles, CA, USA

PUBLICATIONS

JOURNAL PAPERS

1. D. T. Chu, Y.C. Chu, J. A. Lin, Y. T. Chen, C. C. Wang, Y. F. Song, C. C. Chiang, C. Chen, and K. N. Tu, Growth competition between layer-type and porous-type Cu_3Sn in microbumps. Microelectronics Reliability 79, 32-37 (2017).
2. J. A. Lin, C. K. Lin, C. M. Liu, Y. S. Huang, C. Chen, D. T. Chu, and K. N. Tu, Formation mechanism of porous Cu_3Sn intermetallic compounds by high current stressing at high temperatures in low-bump-height solder joints. Crystals 6, 12 (2016).

CONFERENCE PRESENTATION

Y. Wang, D. T. Chu, and K. N. Tu, Porous Cu_3Sn formation in Cu-Sn IMC-based micro-joints. IEEE ECTC Proceedings, pp. 439-446 (2016).

Chapter 1 Introduction

1.1 Overview of the Packaging Technology

Microelectronic industry has two major technologies: chip technology and packaging technology [1]. Electronic packaging provides the connection between silicon chips and outer electronic systems. The most common methods to make chip level interconnections are (1) wire bonding, (2) tape automated bonding (TAB), and (3) flip chip solder bump. Our study addresses issues involved in flip chip solder bump method. For the purpose of comparison, we begin with a brief discussion of the first two methods.

Because of its cost effectiveness and flexibility, wire bonding is most widely used in portable electronic consumer products (such as the mobile phones) for the connection between a Si Chip and a leadframe, which is then electrically connected to the outside circuit. As a typical example, Figure 1-1 shows the bonding of thin wires between a Si chip and a leadframe. The legs of the leadframe are joined to the bond pads on a packaging circuit with solder joints.

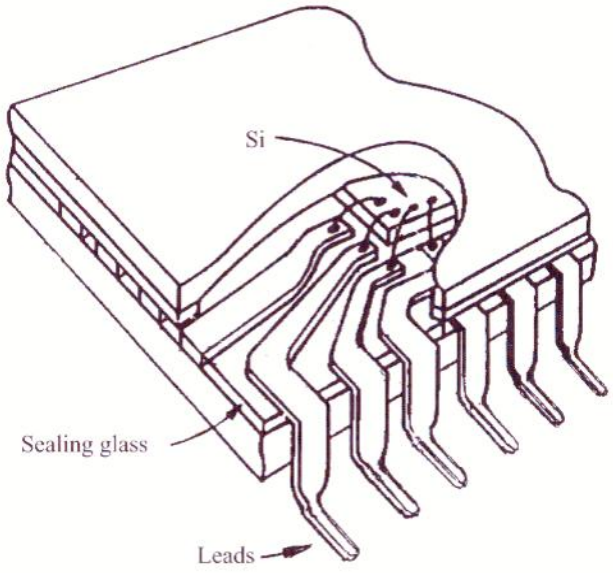

Figure 1-1 Schematic diagram of wire bonding between a Si chip and a leadframe (from Ref. [2], Fig. 1-4).

In tape automated bonding, bare chips are placed onto a printed circuit board by first attaching them to a set of conductors in a perforated polyimide film (Figure 1-2). The film is then mechanically transferred to a location, where the leads are cut and soldered to the board. The TAB facilitates multi-chip module manufacturing. It is a high-volume technology for making the interconnects to silicon devices.

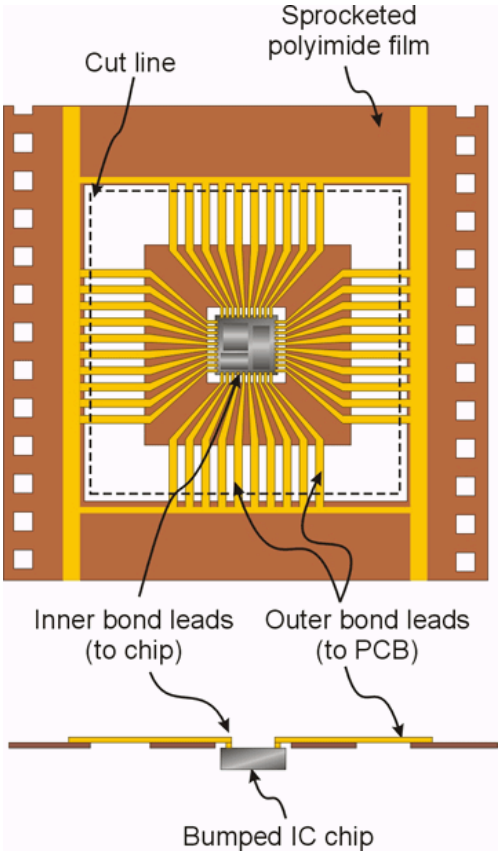

Figure 1-2 Schematic diagram of tape automated bonding (from PC Magazine Encyclopedia).

1.1.1 C4 Flip Chip Packaging

Wire bonding requires ultrasonic vibrations, the stress of which may damage the transistor structures around and underneath the bonded area [2]. Therefore, it can only be done on the periphery of the chip, resulting in the waste of a large fraction of the chip surface.

Assuming 20-μm wires with 20-μm spacing on the periphery of a chip 1 cm^2 in area, we can only have about 1000 I/O joints. This shortcoming is remedied by the flip chip technology, also known as C4 (controlled collapsed chip connection). C4 was invented by IBM in the 1960s [3, 4]. A detailed discussion of the C4 technology and the history of its evolution are reviewed by Puttlitz and Totta [5]. Figure 1-1 summarizes the processing steps for the flip chip. It consists of five basic steps:

1. Integrated circuits are created on the wafer and an area array of bond pads are metalized on the surface of the chip [Figure 1-3(a)].
2. A solder dot is deposited on each of the pads [Figure 1-3(b)]. In this step, the solder bumps are first placed on the chip by evaporation, electroplating, stencil printing, or metal fluid jetting. Then, a reflow process is carried out to connect the solder onto the chip side.
3. Chips are flipped over and positioned so that the solder balls are facing the matching pads on the external circuitry [Figure 1-3(c)].
4. Solder balls are then re-melted or reflow (typically using hot air reflow) [Figure 1-3(d)].
5. Mounted chip is "under-filled" using an electrically-insulating adhesive [Figure 1-3(e)]. Bonding is established by the intermetallic compound layer formed between the pad and the solder.

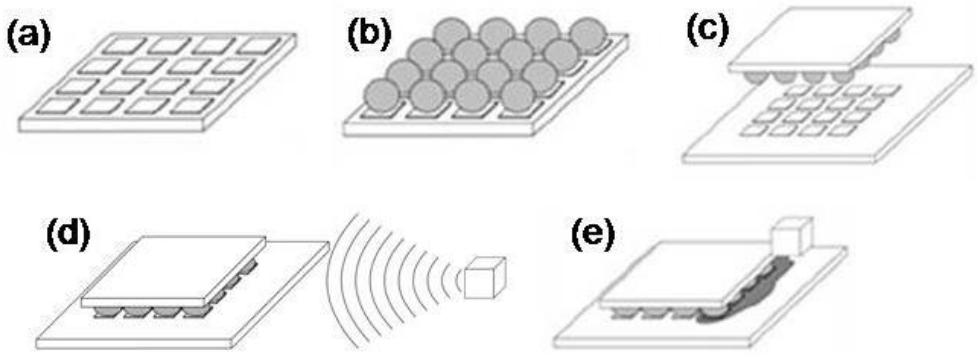

Figure 1-3 Schematic illustration of the processing steps for the flip chip (adaptedfromhttps://en.wikipedia.org/wiki/Flip_chip).

The biggest advantage of the flip chip technology is that an area array of the contact pads can be placed over the entire surface of the chip, instead of being confined to the periphery as in wire bonding [Figure 1-2] and most TAB technologies [Figure 1-3]. Thus, more connections can be made to give more input/output (I/O) joints. Such an area array of tiny solder balls is at present the only practical way for a significant increase of the I/O pads. Assuming 50-μm-diameter solder balls with a 50-μm spacing, we can have about 10,000 I/Os on a 1 cm^2 chip area, representing a tenfold increase in comparison with those of wire bonding just estimated. Because of such an advantage, the 1999 International Technology Roadmap for Semiconductor Technology has identified "solder joint in flip chip technology" to be an important subject of study for its yield in manufacturing and reliability in use [6]. Furthermore, the method also shortens signal interconnections, resulting in an increase in operation speed. For these reasons, while most of the packages utilize wire bond interconnections, the high performance, high I/O count devices increasingly use flip chip.

1.1.2 3D-IC

Moore's law of 2D IC on Si chips has been closely followed for nearly 4 decades due to the miniaturization of transistor size. With the critical feature size down to nm, we are now approaching the physical limit of miniaturization. For further progress, the microelectronic industry is looking into the new direction of 3D IC [1,7, 8].

The 3D structure is achieved by stacking silicon dies onto a 2D package, and interconnecting them vertically with through-silicon-vias (TSVs). The whole stack behaves as a single device to achieve performance improvements at reduced power and smaller footprint. Figure 1-4 is a schematic of a typical 2.5 D package. The difference between 2.5D IC and 3D IC is that the 2.5D IC has an interposer in between the chip and package to reduce thermal stress. If the interposer has no transistors, it is 2.5 D IC. If transistors are built on the interposer, it becomes 3D IC [2]. The ball-grid-array (BGA) bumps at the bottom have a typical size of 760 μm in diameter and the C4 flip chip bumps connecting the chip (or silicon interposer) and packaging substrate are about 100 μm. When it comes to 3D ICs, the size for the microbumps between the stacking chips is down to 10-20 μm.

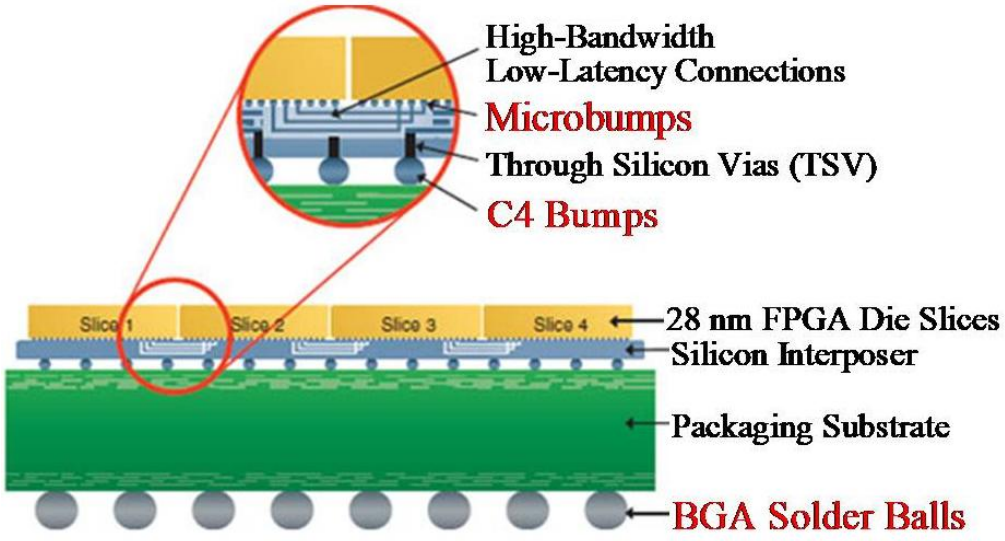

Figure 1-4 Schematic of a 2.5 D package (adapted from Ref. [11]).

3D IC requires an even closer merging of the chip and packaging technologies to meet the new challenges that come with the 2D to 3D transition. For example, the electronic industry is currently developing microbumps [9,10]. The diameter of a microbump is about 10–20 μm, so the density is about 10^5–10^6 joints/cm^2. The microbump has not yet reached the limit in physical size. It is likely that the microbump diameter can be reduced to 1 μm and the density will be 10^7–10^8 joint/cm^2, representing a potential increase by orders of magnitude. Assuming that the Moore's law can be applied to the rate of change of solder joints, it might take 15–20 years to do so, hence this is the new direction of growth or the new paradigm of the future of microelectronic industry [1].

There are numerous applications for 3-D packages in the area of consumer electronic products (for example, medical electronics). In fact, major electronic companies are already developing advanced 3D microelectronic packaging technology in order to meet the trend for portable electronics, which demands ultra-thin structure, ultra-light weight, and high performance with low power consumption.

While the 3D IC is a promising scheme to keep up with Moore's law, it is still a new technology facing many manufacturing and reliability problems. As discussed in [1], in the manufacturing of TSV and micro-bumps, reproducibility and high yield present very serious challenges. For example, the etching of the large-aspect-ratio via holes and the alignment of the vias among the stacking of several chips are non-trivial issues. Challenging issues are also expected in device reliability. For example, due to Joule heating, a large temperature gradient must exist in the packaging, which can lead to thermomigration. Equally challenging reliability issues are electromigration, stress-migration, and chip warpage under compressive stresses. Since details of these reliability problems are mostly unknown, the field of 3D IC offers plenty of research and development opportunities.

1.2 Introduction to Electromigration Test

Formation mechanism of porous Cu_3Sn intermetallic compounds in microbumps is closely related to the phenomenon of electromigartion. Electromigration (EM) is defined as the mass transport from momentum transfer between conducting electrons and diffusing metal atoms. Such a mechanism can result in progressive damage on the metal conductors in an integrated circuit, such as open or short circuit. For electromigration in a metal, the driving force acting on a diffusion atom consists of two forces: (1) electrostatic force, which is the direct action of the electric field on the diffusing atoms, and (2) electron wind force, which is the collision between the moving electrons and the ionic atoms [12]. Their combined force (F) can be written as:

$$F = F_{direct} + F_{wind} = Z^{*}eE = (Z_d^{*} + Z_{wd}^{*})eE \quad (1)$$

In Eq. (1), Z^* is the effective charge number, e is the electron charge, and E is the electric field. The effective charge Z^* contains two terms: Z_d^* and Z_{wd}^*. Z_d^* is nominal valence of the diffusing ion in the metal when the dynamic screening effect is ignored, while Z_{wd}^* is the effective charge number representing the effect of momentum exchange between the electrons and the diffusing ion. So the term Z_d^*eE is the direct force which draws atoms towards the negative electrode. On the other hand, Z_{wd}^*eE, called the electron wind force, is the force resulting from the collision between the moving electrons and the diffusion ion. The electron wind force component is generally the dominant term and is found to be 10 times higher than the electrostatic force in a good conductor like Ag, Al, Cu, Pb, and Sn, etc. With the effect of EM, the atomic flux equation is as follow:

$$J = J_{chem} + J_{em} = -D\frac{dC}{dx} + C\frac{D}{kT}Z^{*}eE \quad (2)$$

where C is atomic concentration, D is the atomic diffusivity, k is Boltzmann's constant, and T is the temperature. In Eq. (2), the atomic flux J consists of two terms: J_{chem} and J_{em}. J_{chem} is the

atomic flux driven by the concentration gradient, whereas J_{em} is the flux generated by electromigration.

1.3 Motivation

In the pursuit of higher operation speed and improved performance of microelectronic devices, the application of flip chip solder joints has become a key technology for high-density packaging [13]. The solder joints have been used in high power devices, such as central processing unit (CPU) and application processors (AP). The specified operation temperatures for these devices range from 100 °C to 110 °C and the required lifetime is usually 10 years. To meet the demand for portable devices, the input/output pin numbers continue to increase while the size of the solder joints continues to shrink. This inevitably leads to higher current densities and operating temperatures in the joints. Therefore, it raises serious reliability issues such as electromigration (EM) and thermomigration [14].

Dimensional shrinkage of the solder joints in portable devices may cause new reliability issues. When the Cu and solder are put together at an elevated temperature the intermetallic compound (IMC) forms in-between to make a joint. When the IMC layers reaches about 10 μm thick, it becomes a diffusion barrier for Cu to diffuse across, so the growth slows down greatly. In a C4 bump, the IMC only occupied a small portion of the bump (Figure 1-5, left). However, when the bump size is down to 20 μm as for the microbump, the whole bump tends to be transformed into an IMC bump during electromigration tests [15] (Figure 1-5, right). Its properties are not the same as what we have studied before in C4. The IMC is strong but brittle, so it will cause new kinds of reliability issues.

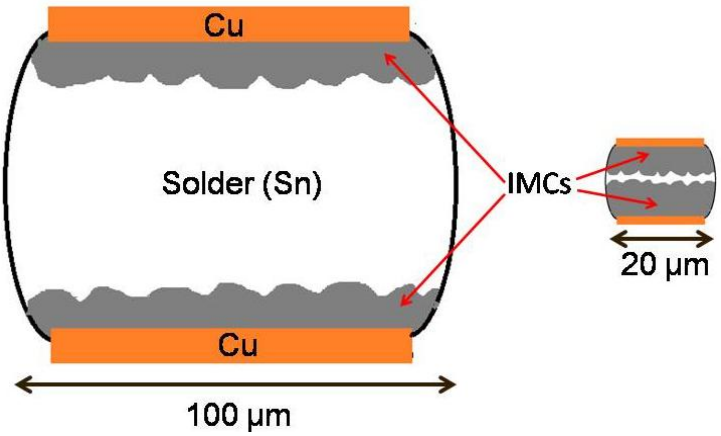

Figure 1-5 A schematic showing how smaller solder joints tend to transform completely into IMC joints during EM test.

Additionally, in low-bump-height solder joints, when they are combined with a thick column-type Cu UBM, the solder reaction on the side wall of the Cu-column becomes one of the new reliability issues of concern. For example, Liang *et al*. found that, in reflow tests, the effect of side wall reaction would lead to the formation of large voids in the solder joints [16].

Over the past decades, electromigration behavior and metallurgical reactions of flip chip solder joints have been widely studied [17-22]. The intermetallic compounds (IMC) of Cu_3Sn and Cu_6Sn_5 are commonly formed in solder reactions on Cu under-bump-metallization (UBM). The formation of Cu_6Sn_5 and Cu_3Sn is essential in providing the metallic bonding between the Cu and solder. On these two IMCs, the growth of Cu_6Sn_5 has been studied widely. This is because it is the first phase to form in the wetting reaction of molten solder on Cu. Even when the eutectic SnPb is replaced by the Pb-free SnAgCu, Cu_6Sn_5 remains to be the first phase to form. Upon a longer reflow or a long time solid state aging, a layer-type Cu_3Sn will form between Cu_6Sn_5 and Cu.

On the other hand, in the recent trend of device minimization for mobile consumer electronic products, the size or the thickness of solder joints is being reduced to 20 μm or less. In these so-called microbumps, a new morphology of Cu_3Sn, the porous-type, has been found [24-28]. In the earliest of such studies [24], Panchenko *et al*. reported the formation of a porous structure [Figures 1-6(a) and 1-6(b)] in 50 μm pitch Cu/Sn microbump interconnects during reflow due to the degradation of the Cu_6Sn_5 IMCs layer. Energy dispersive X-ray (EDX) spectroscopy confirmed that the porous structure was Cu_3Sn [Figure 1-6(c)].

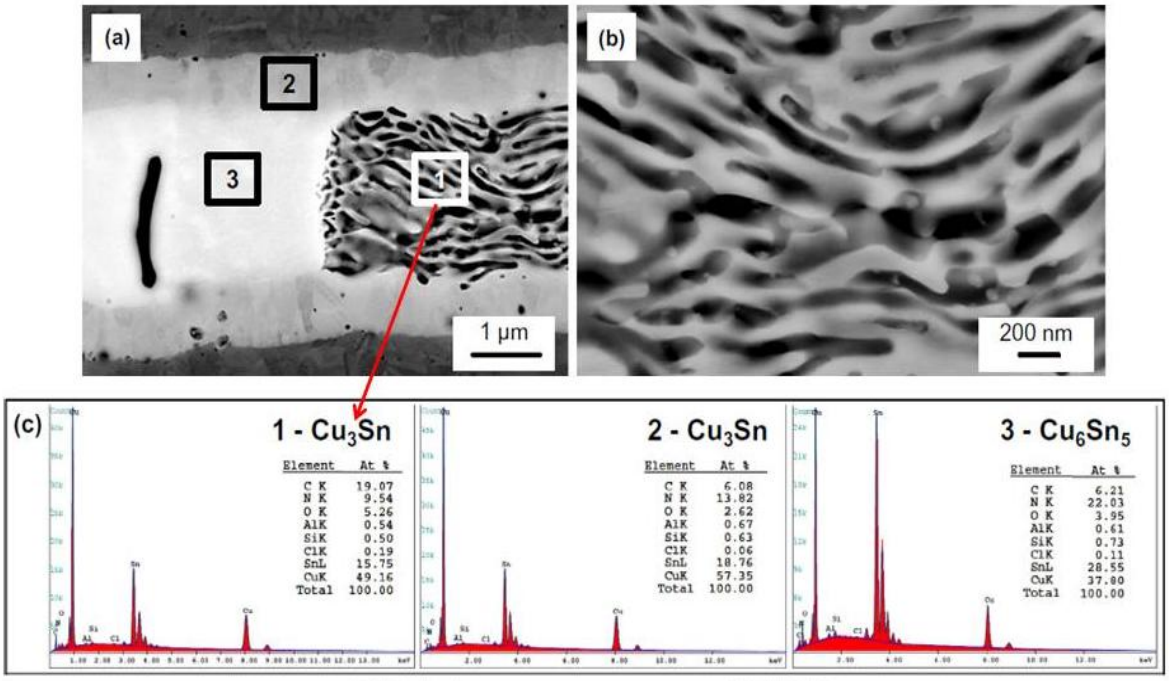

Figure 1-6 EDX analysis on the Cu/Sn microbump interconnect: (a) EDX spectra regions; (b) Magnified backscatter image of the pore region; (c) EDX spectra for regions 1, 2, and 3 in (a) (from Ref. [24]).

While the layer-type Cu_3Sn is known to contain a small amount of Kirkendall voids [29-31], the porous Cu_3Sn has a much larger fraction of voids, near 40%. In Ref. [24], the proposed explanation of the porous Cu_3Sn formation is the dissolution of Sn atoms from the Cu_6Sn_5 matrix owing to the reaction between Cu_6Sn_5 and flux residues, or the diffusion of the Sn atom to the sidewall.

However, the formation mechanism of the porous Cu_3Sn structure has not yet been fully understood. Many questions need to be answered. For example, what is the dominant mechanism in porous structure formation? Can the porous structure form under current stressing? What are the parameters affecting the porous structure formation? Therefore, in this thesis, we attempt to provide some answers to these questions, in experiment and in theory. In subsequent chapters, we will propose a detailed formation mechanism of the porous Cu_3Sn. EM tests will be performed to determine the conditions for porous Cu_3Sn formation under current stressing - the use condition of most electronic devices. Parameters affecting porous structure formation will also be examined. Finally, a kinetic analysis of this complete precipitation process will be presented and compared with the classical case of incomplete precipitation.

1.4 Main Diagnostic Tools of Research

1.4.1 Scanning Electron Microscope (SEM)

A microscope is characterized by two basic parameters: magnification and resolution. The magnification refers to the ratio of the image size to the actual sample size, while the resolution is the minimum distance between two points of the sample, whose images are still distinguishable as separate points. The optical microscope has a magnification up to approximately 1000. However, its resolution is limited to approximately 200-250 nm. This is

a length comparable to the wavelength of visible light (400-700 nm), which is the minimum size of an optical focal point**.** On the other hand, the electron as a matter wave has a much shorter wavelength. For example, an 1-eV electron has a wavelength of 1.23 nm and it decreases linearly with an increase in electron momentum. Thus, an electron beam can be focused (usually by magnetic fields) to nm size to provide a resolving power better than 1000 times of that of the optical microscope. In addition, the magnification has a wide range, from about 10 to greater than 500,000.

There are two major types of electron microscope: scanning electron microscopy (SEM) and transmission electron microscopy (TEM). In either type, an electron beam focused by an electromagnetic lens is used to scan the sample. The SEM electron beam scans the sample surface and interacts with atoms to produce various signals. In the most common SEM, the secondary electrons emitted by atoms are detected, the number of which contains information about every emitting point. The scanning beam thus generates an image of the sample's microstructure and composition. In the TEM, the electron beam passes through a thin sample, where the electrons are absorbed or diffracted. The variations in electron intensity are eventually converted into sample images. TEM produces two-dimensional images that are useful for studying the sample's internal structure.

The SEM used for our study is Model JEOL JSM-6500 F (Figure 1-7) in the facility of National Chiao Tung University (NCTU). It is a field emission scanning electron microscope. Backscatter electron mode was selected to image most of the IMG containing samples due to its better contrast of different materials.

Figure 1-7 The scanning electron microscopy (Model JEOL JSM-6500 F) at NCTU.

1.4.2 Synchrotron Radiation Imaging–Transmission X-Ray Microscopy

In addition to cross-sectional SEM imaging, the porous structures will also be examined by X-ray microscopy, which is a technique complementary to optical and electron microscopy. Because of its deep penetration depth into matter and its non-destructive nature, the X-ray microscope has been widely used for the analysis of failure mechanisms in microelectronic devices due to electro-migration, thermal breakdown, or inhomogeneity. It is also a useful tool for the characterization of porous materials and the investigation of their transportation behavior.

A high-energy electron in circular motion emits a narrow beam of X-ray in the direction of electron motion. This effect is widely exploited in synchrotrons in which bunches of

circulating electrons (typically 1-3 GeV in energy) produce X-rays of unprecedented intensity for diagnostic purposes. For example, at the Advanced Light Source (ALS) in Berkeley, a soft X-ray (100 eV–1 keV) transmission microscope has achieved a spatial resolution as high as 15 nm [32]. The resolution is generally lower in the hard X-ray regime due to fabrication difficulties. On the other hand, hard X-rays allow the imaging of thick samples (hundreds of μm) and their spatial resolution is improving steadily.

In particular, a transmission X-ray microscope in the energy range of 8-11 keV has been constructed at the National Synchrotron Radiation Center (NSRRC) in Taiwan. It provides 2D imaging and 3D tomography with a spatial resolution close to 60 nm [33]. We have obtained images of our porous Cu_3Sn samples by 3-D tomography in the BL01B1 beamline of this facility [34]. The optical assembly of the transmission X-ray microscope at the end of the beamline is shown in Figure 1-8.

Figure 1-8 The optical assembly of the transmission X-ray microscope at NSRRC.

Chapter 2 Porous Cu_3Sn Formation under Current Stressing

As discussed earlier, the intermetallic compounds (IMC) of Cu_3Sn and Cu_6Sn_5 are commonly formed in solder reactions on Cu under-bump-metallization (UBM). The Cu column-type UBM (a structure with a thicker Cu) was developed to alleviate both the Joule heating and current crowding effects in flip-chip solder joints under normal device operating conditions. In this chapter, we investigate the microstructure evolution of solder joints with Cu column UBM, especially the porous Cu_3Sn formation, under current stressing at 1.45×10^4 A/cm^2 at 185 ^{o}C and 1.20×10^4 A/cm^2 at 0 ^{o}C.

2.1 Experimental

Typical flip-chip solder joints were used in our electromigration tests. Figure 2-1(a) shows the schematic diagram of a bump with Cu column UBM. On the chip side, 100 nm Ti was sputtered as the adhesion layer. Then a 2 μm Cu layer was sputtered as the seed layer for the subsequent electroplating of a 50 μm Cu UBM column and SnAg solder. The composition of the solder was Sn-2.3Ag. The diameter of UBM and passivation opening is 145 and 85 μm, respectively. The Cu trace on the flame retardant 5 (FR5) substrate is 100 μm wide and 27 μm thick. Pre-solder of Sn-2.3Ag was used on the substrate side. The chips were flipped over to align with the substrates, and they were reflowed at 260 ^{o}C for 1 min to form flip-chip solder joints. Figure 2-1(b) illustrates the cross-sectional SEM images of a flip-chip bump before the electromigration EM tests. A scallop-type Cu_6Sn_5 layer was found at the interface between the Cu metallization and the solder on the chip side, as well as on the substrate side [2].

Four-point probes were employed to monitor the resistance change during the EM tests of the bump. Figure 2-1(c) presents the schematic of the test layout. There are 6 nodes (n1 to n6) in the test layout, and the direction of the electron flow is pointed by the red arrows which

shows the two bumps (b1 and b2) were stressed with opposite direction of electron flow. The electrons enter from n1, go upward through b1, then downward through b2, and finally flow out from n6. The resistance change in b1 (b2) can be measured by the voltage drop between n2 and n3 (n5 and n6). In the microelectronic industry, a failure is typically defined when the resistance change increases to 20% of its initial value [35]. In our study, the early stage of the tests was defined when the bump resistance increment is smaller than 20% during the EM tests, while the later stage of test was defined when the increment was larger than 20%.

The solder joints were stressed with 2.4 A and 2 A at 150 ^{o}C. The calculated current densities were 1.45 × 10^4 A/cm^2 and 1.20 × 10^4 A/cm^2, respectively, based on the UBM opening size. The real temperature in solder joints may be higher than the ambient temperature during current stressing due to Joule heating effect in the stressing condition [20]. Therefore, in our study the temperature coefficient of resistivity (TCR) were employed to measure the real temperature in the joints. The calibrated temperatures were about 185 ^{o}C and 170 ^{o}C when the test sample was stressed with 2.4 and 2 A, respectively.

Solder joints were cross-sectioned by grinding using abrasive papers #400, #1000, #2000, #2500, and #4000, and then polished by Al_2O_3 of 1 and 0.3 μm. The microstructure and composition were examined with a JEOL 6500 field-emission scanning electron microscope (SEM) (JEOL Ltd., Tokyo, Japan) and energy dispersive spectroscopy (EDS) (Oxford Instruments, Oxfordshire, UK). The SEM EDS was operated at 15 KeV with a current of 1.0 × 10^{-5}A and a beam size of 1000 nm. Focused ion beam (FIB, FEI Nova 200, FEI Company, Hillsboro, OR, USA) technique was adopted for cross-sectional observation, and transmission electron microscopy (TEM, JEOL-2100F, JEOL Ltd., Tokyo, Japan) and electron probe micro-analyzer (EPMA, JXA-8800M, JEOL Ltd., Tokyo, Japan) were utilized to verify the

microstructure results. The operation conditions for the EPMA were at 12 KeV with a current of 1.0×10^{-8} A and a beam size of 500 nm.

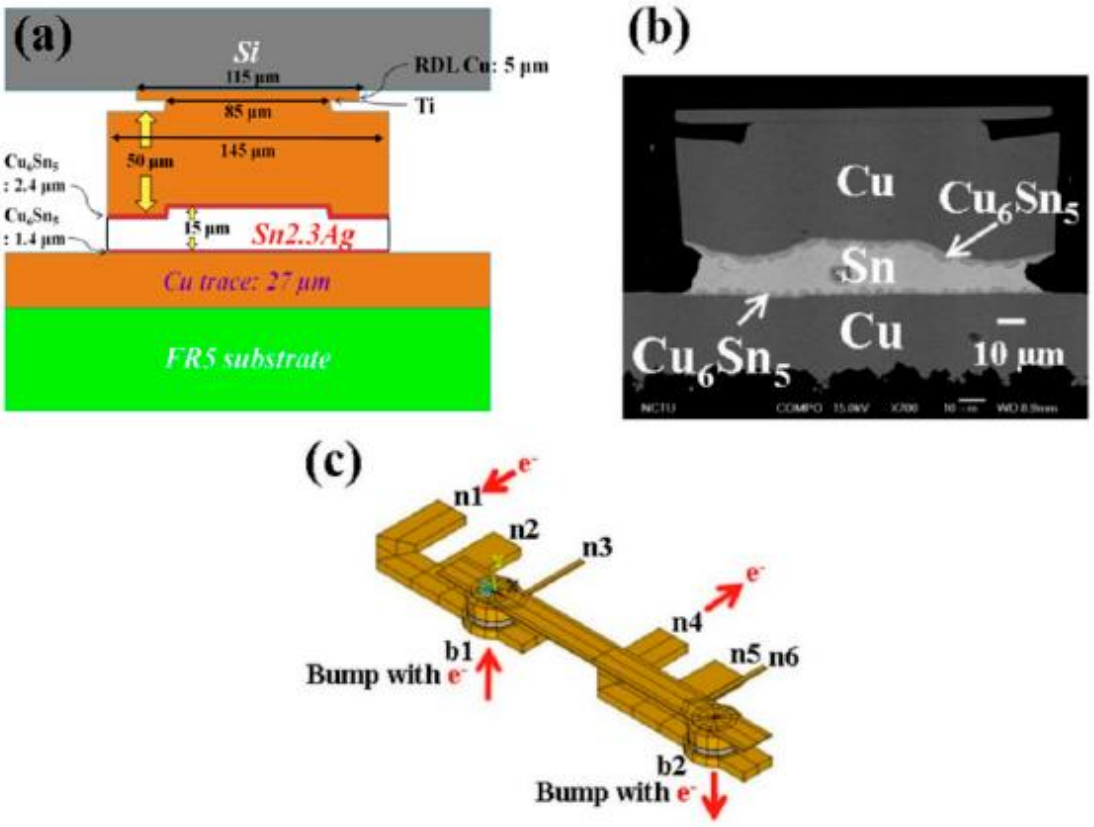

Figure 2-1 (a) Schematic of the flip-chip solder joints with Cu column UBM. The redistribution layer (RDL) on the Si chip is 5-μm thick Cu. (b) Cross-sectional SEM images. (c) Layout for electromigration tests and four-point structure for measuring bump resistance.

2.2 Results and Discussion

2.2.1 Current-Enhanced IMC Formation

The formation of Cu-Sn IMCs can be significantly enhanced by current stressing. Figure 2-2 shows cross-sectional SEM images of a pair of solder joints stressed with $1.45 \times 10^4 A/cm^2$ at 185 ^oC. At the early stage, the bump resistance increased by 5% (after 283 h in the upward electron flow) and 10% (after 283 h in the downward electron flow) of its initial value, are shown in Figures 2-2(a) and 2.2(b), respectively.

The current enhanced the dissolution of Cu UBM to react with the solder joint and form a large volume of IMCs. The layer-type Cu_6Sn_5 formed in the middle of the bump and the layer-type Cu_3Sn formed at the interfaces between the Cu and Cu_6Sn_5. The entire joint almost completely transformed into IMC joints at the early stage in the EM tests, although there was still some Sn remaining in the bump, as indicated in Figure 2-2(b). The results showed that a large volume of IMCs formed at the early stage regardless of the direction of the electron flow.

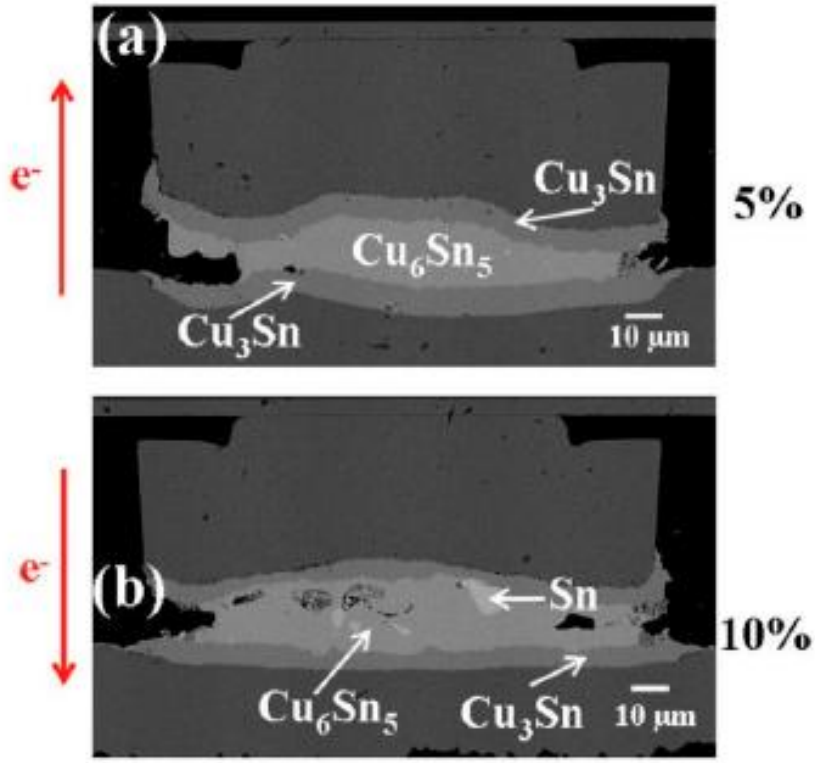

Figure 2-2 Cross-sectional SEM images of solder bumps with Cu column UBM stressed at 1.45×10^4 A/cm^2 and 185 ^{o}C with bump resistance increases of (a) 5% with upward electron flow and (b) 10% with downward electron flow.

2.2.2 Formation of Porous Cu3Sn

It is interesting that porous Cu_3Sn IMCs may form at later stages of electromigration tests. Figures 2-3 and 2-4 illustrate the cross-sectional SEM images at different stages in the EM tests with opposite direction of electron flow. Figure 2-3 shows the EM test results with upward electron flow. Figures 2-3(a)–(c) are the cross-sectional SEM images with bump resistance increase, 8% (after 517 h), 32% (after 217 h), and 85% (after 429 h) of its initial value, respectively. When the bump resistance increased to 8% of its initial value, the layer-

type Cu_6Sn_5 in the middle started to transform into porous-type Cu_3Sn, as shown in Figure 2-3(a). We note that the porous-type Cu_3Sn first formed on the periphery of the bump. As the change in bump resistance increased to 32%, shown in Figure 2-3(b), the layer-type Cu_6Sn_5 IMC had fully transformed into porous-type Cu_3Sn IMC. Figure 2-3(c) shows similar results from a different bump, as in Figure 2-3(b) which means the Cu_6Sn_5 IMC had also totally transformed into porous-type Cu_3Sn IMCs in the later stage of the EM tests.

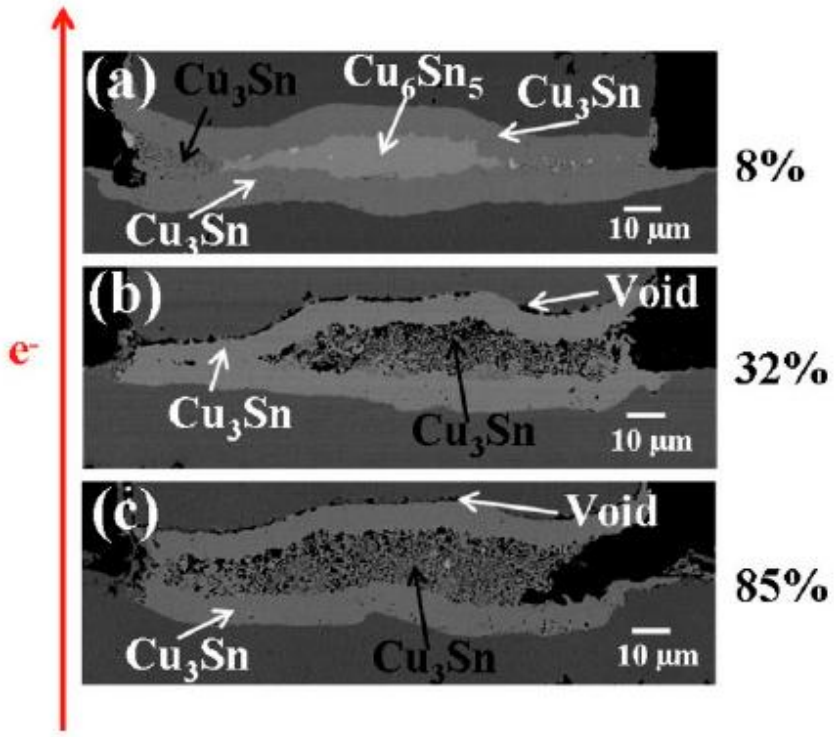

Figure 2-3 Cross-sectional SEM images of solder bumps with Cu column UBM stressed at 1.45×10^4 A/cm^2 with upward electron flow at 185 ^{o}C with bump resistance increases of (a) 8%, (b) 32%, and (c) 85% of its initial value.

Similarly, Figure 2-4 shows the EM tests results with downward electron flow, where Figures 2-4(a)–(c) illustrate the cross-sectional SEM images with the bump resistance increase 15% (after 517 h), 20% (after 217 h), and 100% (after 429 h) of its initial value,

respectively. The results are similar to those in Figure 2-3. As the bump resistance increased, the layer-type Cu_6Sn_5 in the middle started to transform into porous-type Cu_3Sn.

In order to rule out the possibility that the porous structure was generated in the polishing processor by other external forces, FIB were utilized to provide a deeper cross-section in a selected solder joint, stressed at 1.45×10^4 A/cm^2 for 429 h as illustrated in Figure 2-5. The downward direction of the electron flow was labeled in the figure. This second cross-section view indicated that the porous structure not only formed on the polished surface but in the entire bump.

In the bumps with porous Cu_3Sn, we observed that the effect of side wall reaction is very serious. Park *et al*. reported that a high stressing current may lead to a serious side wall reaction effect [36]. Figure 2-6(a) shows the side wall of a bump. The bump has had porous-type Cu_3Sn IMCs formation. We can clearly observe that there are IMCs formation on the side wall, indicated by the ellipses. Since the thickness of the IMCs formed on the side wall is only about 3 μm, it is hard to verify the composition with EDS. Hence, EPMA was used instead. Figure 2-3(b) illustrates the results that all the IMCs formed on the side wall are Cu_3Sn. The compositions of the layer-type and porous-type structures were also confirmed with EPMA to be Cu_3Sn, identical with the results measured with EDS. Therefore, the whole joint has transformed completely into Cu_3Sn with two different morphologies.

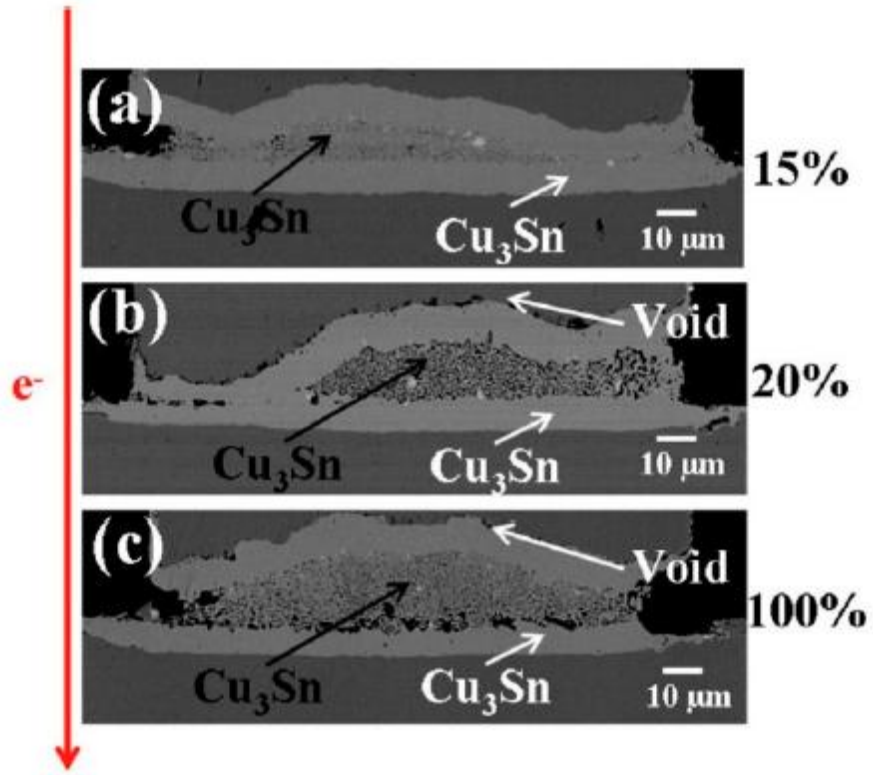

Figure 2-4 Cross-sectional SEM images of solder bumps with Cu column UBM stressed at 1.45×10^4 A/cm^2 with downward electron flow at 185 °C with bump resistance increases of (a) 15%, (b) 20%, and (c) 100% of its initial value.

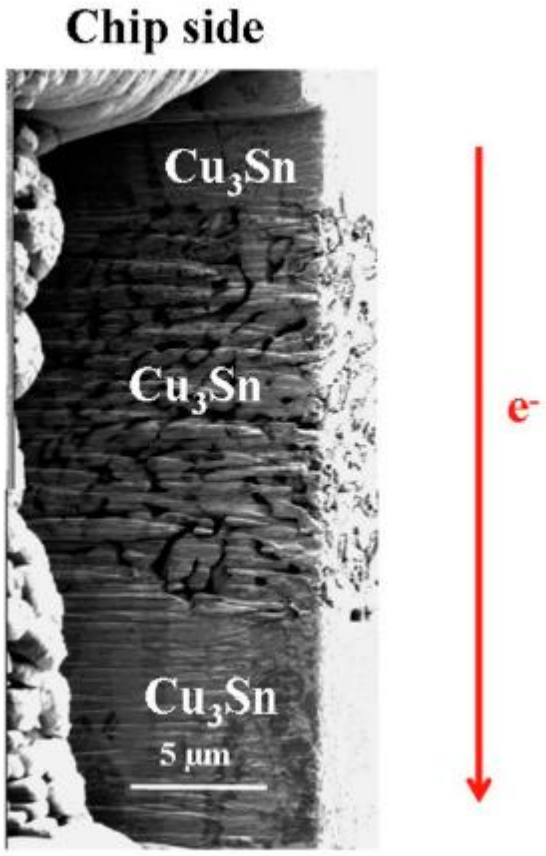

Figure 2-5 Cross-sectional FIB image of Cu_3Sn IMC structures.

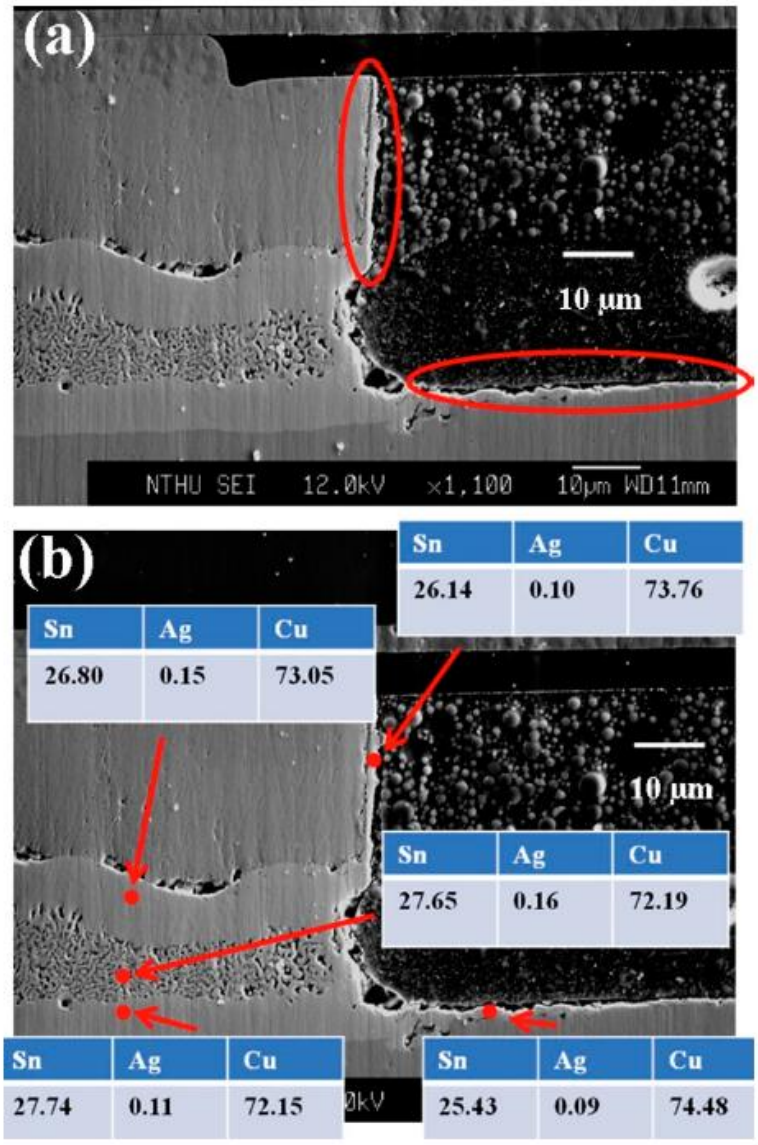

Figure 2-6 Cross-sectional SEM images of (a) IMCs formed on the side wall and (b) EPMA analysis. The composition data were shown in atomic percent.

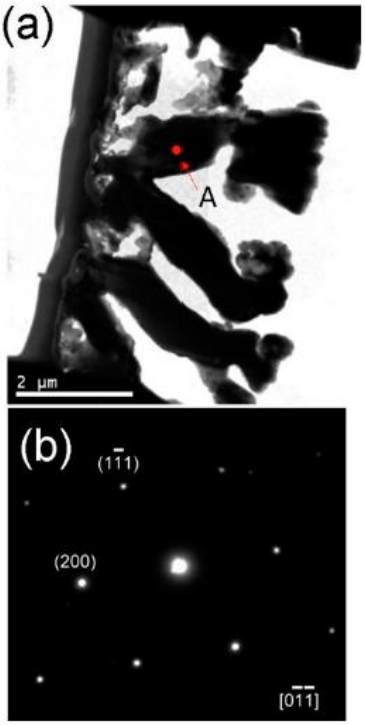

Figure 2-7 (a) Cross-sectional TEM image of porous-type structure and (b) diffraction patterns of point A in (a).

Figure 2-8 shows cross-sectional SEM images of a pair of solder joints stressed with 1.2 × 10^4 A/cm^2 at 170 °C. The bump resistance increases 140% (after 5094 h) and 530% (after 5094 h) of its initial value as indicated in Figure 2-8(a) and Figure 2-8(b), respectively.

It can be seen that only layer-type Cu_3Sn and layer-type Cu_6Sn_5 have formed, with no evidence of porous Cu_3Sn even in the case of Figure 2-8(b). The results demonstrate that the solder joints do not transform into porous structures at an insufficient current density and temperature.

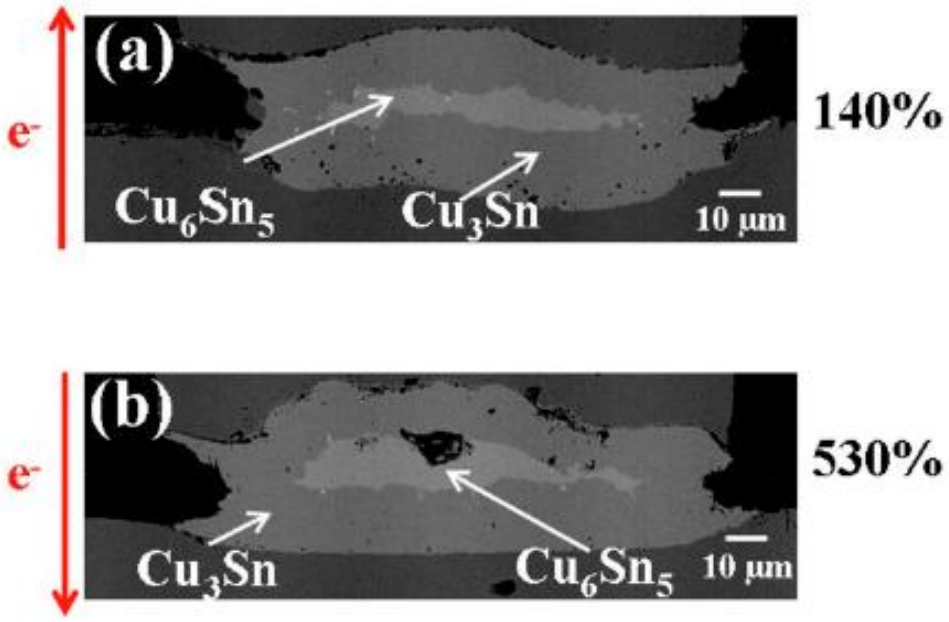

Figure 2-8 Cross-sectional SEM images of solder bumps with Cu column UBM stressed at 1.20× 10^4 A/cm^2 and 170 °C with bump resistance increases of (a) 140% with upward electron flow and (b) 530% with downward electron flow.

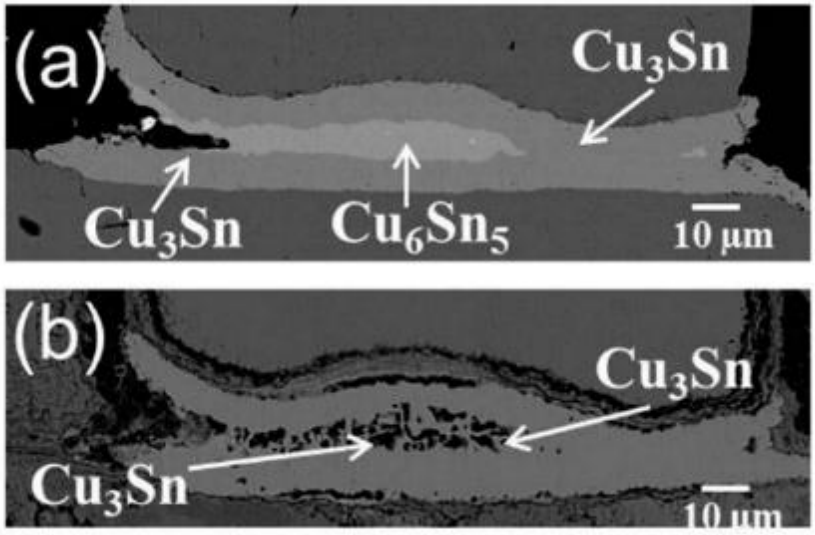

Figure 2-9 Cross-sectional SEM images of solder bumps with Cu column UBM aging at 185 °C for (a) 1000 h and (b) 2000 h.

To further examine the temperature effect on porous Cu_3Sn formation, another set of bumps were aged at 185 °C in the oven without current stressing. In the case of 1000-h aging [Figure 2-9(a)], the joints have fully transformed into IMC joints. Layer-type Cu_6Sn_5 has formed in the middle of the bump and layer-type Cu_3Sn has formed between Cu and Cu_6Sn_5. In the case of 2000 h aging [Figure 2-9(b)], the layer-type Cu_6Sn_5 in the middle has completely transformed into porous Cu_3Sn. The results show that porous Cu_3Sn could form without current stressing at a sufficiently high temperature, which gives an independent confirmation of temperature's critical role in the formation of porous Cu_3Sn.

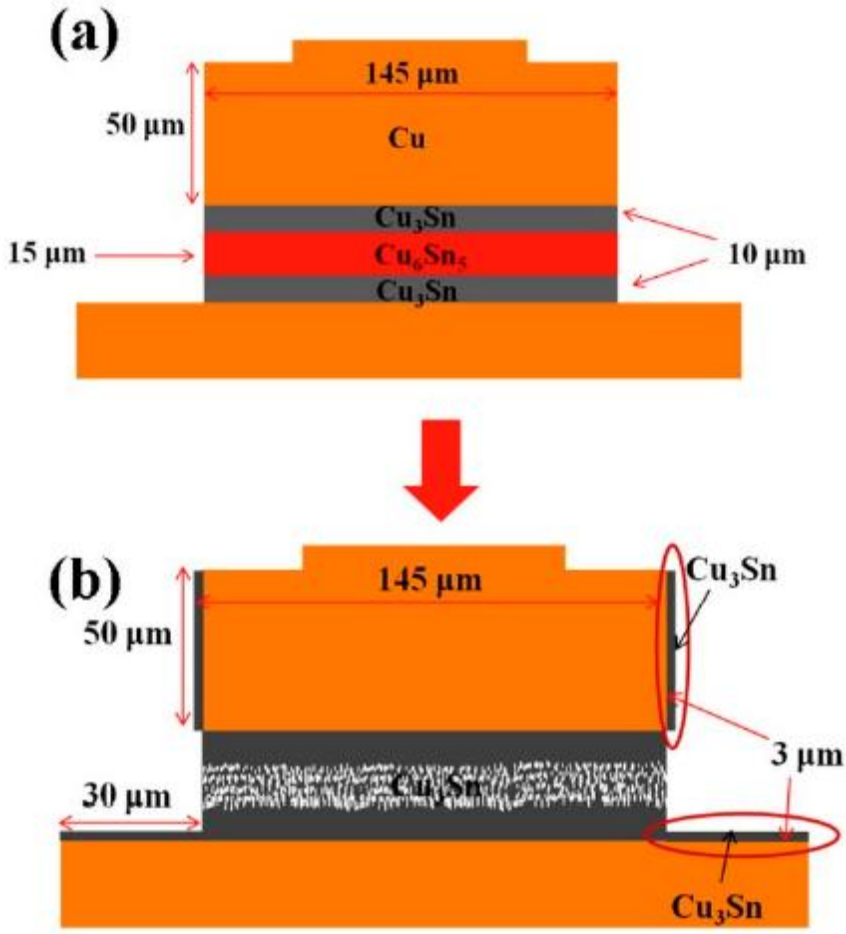

Figure 2-10 Schematic diagrams of transformation process at (a) early stage and (b) final stage in the electromigration tests.

2.2.3 Formation Mechanism of Porous Cu_3Sn IMCs

On the formation mechanism of porous Cu_3Sn, first, the temperature must be high enough and, second, the solder height must be low enough so that the Cu supply is enough for the whole joint to transform into IMC. This is because when there are unreacted solders in the joints, the major IMC is Cu_6Sn_5 after the metallurgical reactions, as illustrated in Figure 2-1(b). Only a thin layer of Cu_3Sn presented between the Cu metallization layer and the Cu_6Sn_5 IMCs. The transformation process is schematically illustrated in Figure 2-10. In the early stage of the EM tests, layer-type Cu_6Sn_5 and Cu_3Sn formed first, as shown in Figure 2-10(a). As the bump resistance increased, the layer-type Cu_6Sn_5 started to transform into porous-type Cu_3Sn, as illustrated in Figure 2-10(b). The IMCs formed on the side walls due to the effect of side wall reaction are also shown in Figure 2-10(b), labeled by the ellipses.

According to the experimental results, we have developed the following mechanism to explain the formation mechanism of the porous-type Cu_3Sn. Previously, the Kirkendall void formation mechanism in Cu_3Sn was proposed [31]. When the layer-type Cu_6Sn_5 decomposes into Cu_3Sn, it will release 3 Sn atoms:

$$Cu_6Sn_5 \rightarrow 2Cu_3Sn + 3Sn \quad (3)$$

The 3 Sn atoms released in Eq. (3) will then attract nine Cu atoms to form three more Cu_3Sn.

$$3Sn + 9Cu \rightarrow 3Cu_3Sn \quad (4)$$

The vacancies which enable the diffusion of the Cu atoms tend to form Kirkendall voids in Cu_3Sn. It implies that the growth of layer-type Cu_3Sn IMCs is at the expense of layer-type Cu_6Sn_5 IMCs. However, in our experimental results, it can be observed that as the layer-type Cu_3Sn IMCs grew to a certain thickness, the layer-type Cu_6Sn_5 would not transform into the layer-type but porous-type Cu_3Sn. Hsiao *et al.* found that Cu-Sn IMCs can become a diffusion

barrier for the Cu/solder reaction [37]. We assume that the layer-type Cu_3Sn served as a diffusion barrier and inhibited the Sn atoms released from the decomposition of Cu_6Sn_5 to react with Cu. Since the bumps were stressed with high current density at high temperature, the released Sn diffused to the side wall to form Cu_3Sn due to the effect of the side wall reaction. The place originally occupied by Sn became empty and led to the porous type structure.

2.2.4 Polarity Effect

We have observed the polarity effect in the final stage of the EM tests; namely, more porous structures formed on the anode side than on the cathode side. Two identical microbump samples were stressed at the same current of 2.2×10^5 A/cm^2 but at different temperatures.

The first sample was stressed on a 100 °C hotplate and the temperature in the bump was 130 °C with joule heating. Under this condition, the porous structure will not form due to insufficient temperature. As shown in Figure 2-11, there are some voids formed on the anode side of the bumps, which are the results of current stressing (EM) alone.

The second sample was stressed on a 150 °C hotplate (180 °C with joule heating). At this temperature, porous structure can form with the assistance from the current, as shown in Figure 2-12. The porous structure is in a trapezoid shape, which is the combined result of the outward chemical force and upward (downward) EM force. The dissolved Sn atom is moving in the direction of the vector sum of these 2 forces, as shown in Figure 2-13.

By the mechanism theorized above, the phenomenon was caused by an abundant Cu supply on the cathode side than on the anode side. Hence, there was more Cu_3Sn formation on the cathode side. However, Cu atoms were less likely to diffuse to the anode side to react with

the released Sn. As a result, the porous structure was more obvious on the anode side. The polarity effect is, thus, a consequence of the proposed mechanism.

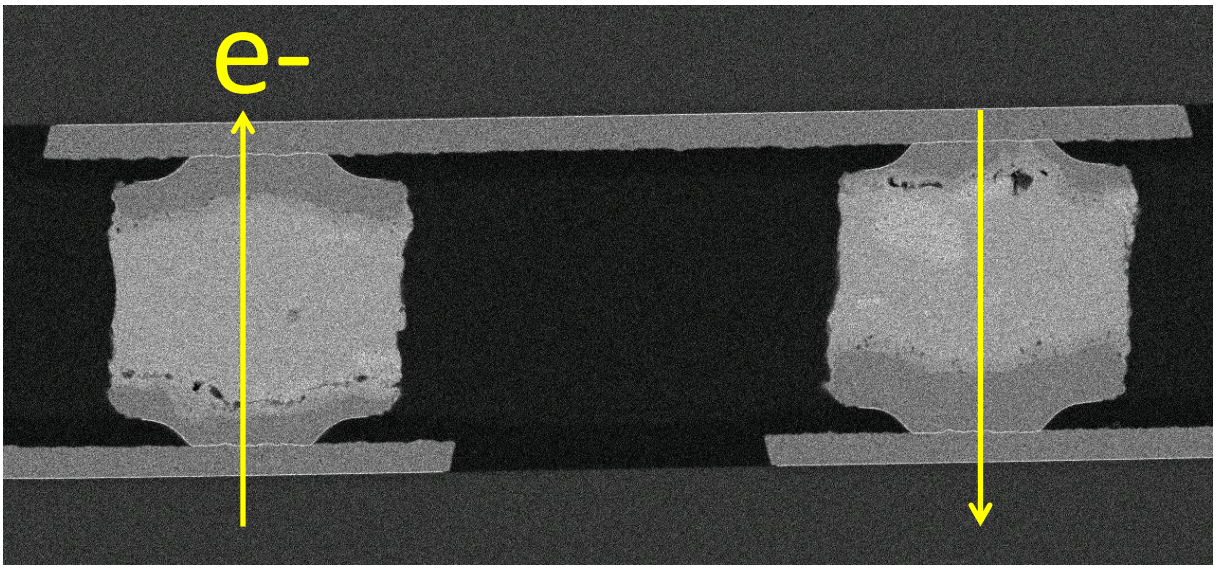

Figure 2-11 A set of 2 microbumps stressed at 2.2×10^5 A/cm^2 on a 100 °C hotplate.

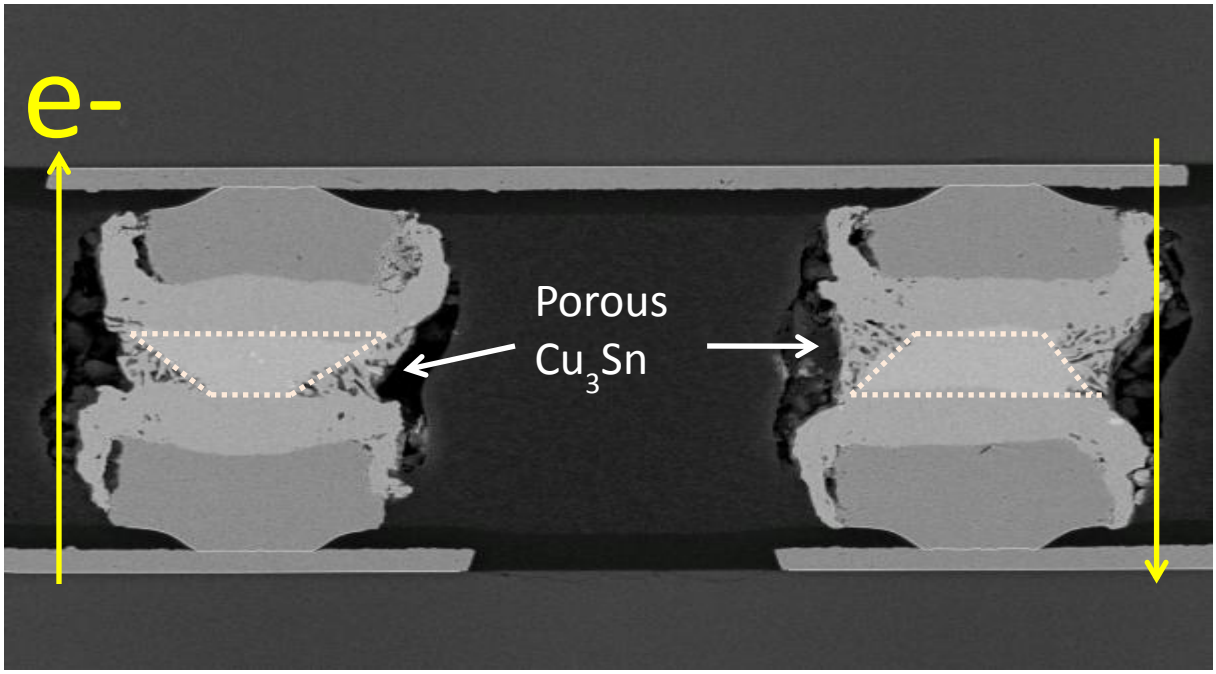

Figure 2-12 A set of 2 microbumps stressed at 2.2× 10^5 A/cm^2 on a 150 °C hotplate.

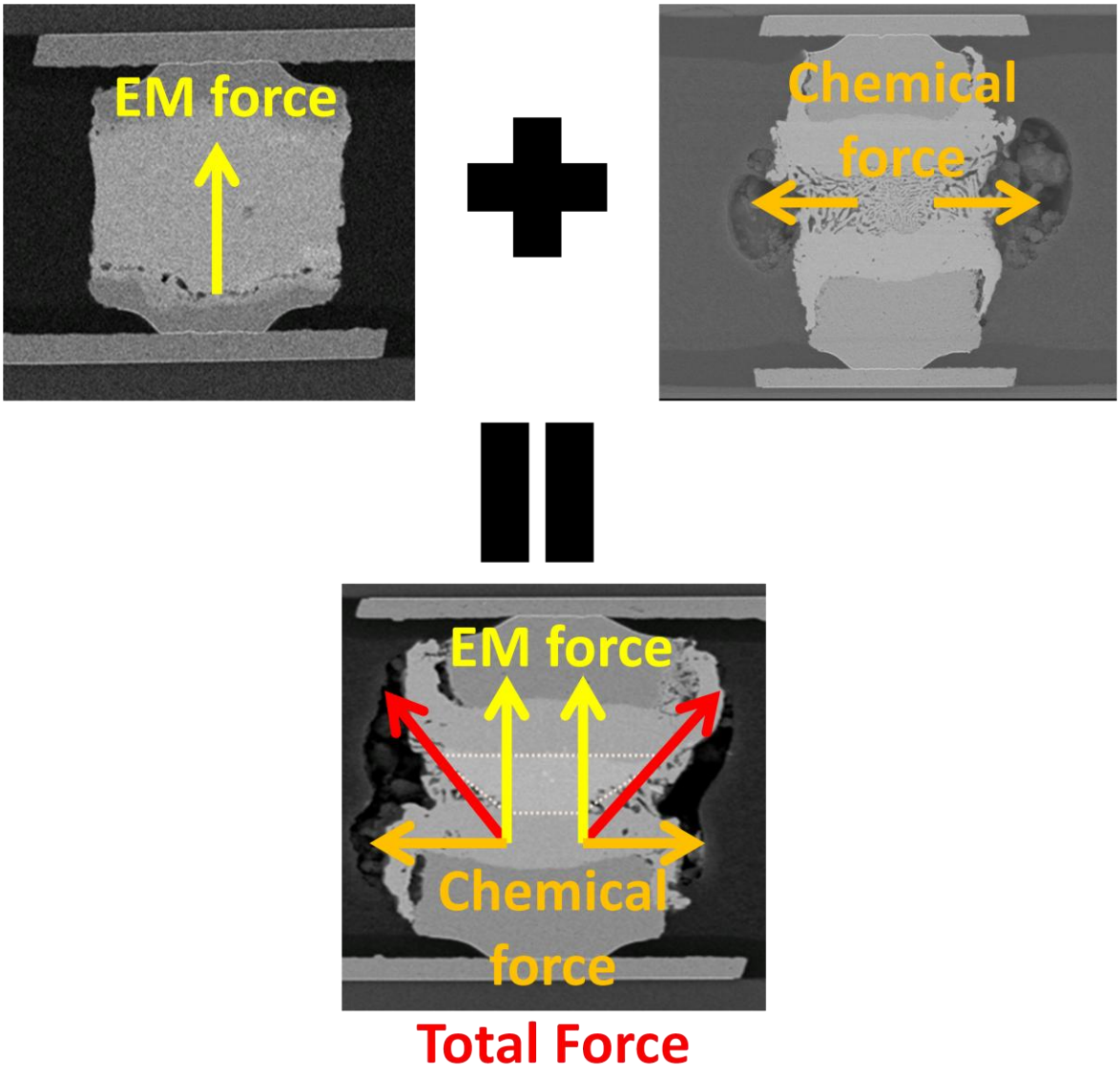

Figure 2-13 Explanation of the trapezoid shape as a combined result of the outward chemical force and upward (downward) EM force.

2.2.5 Theoretical Calculation of the Pore Volume

This mechanism can be further verified by volume calculations. One mole of Cu_6Sn_5 decomposes into two moles of Cu_3Sn plus three moles of Sn. Approximately, one mole of Cu_6Sn_5 has a volume of 117.7 cm^3, two moles of Cu_3Sn has a volume of 69.5 cm^3, and three moles of Sn has a volume of 48.4 cm^3. In our observation, the volume before and after the Cu_6Sn_5 to Cu_3Sn conversion was nearly unchanged (117.7 to 117.9 cm^3). Calculations also indicate that the volume change in phase transformation is negligible.

On the other hand, the diffusion of Sn to the side walls would leave the pores behind. Assuming that the pore volume equals that of the released Sn, we have calculated the volume occupied by pores to be 41.2% (48.4/117.9) of the porous Cu_3Sn volume, when all the released Sn atoms diffuse to the side walls of the UBMs. As a verification, we have used software to calculate the volume percentage of the pores in the actual bumps. Six bumps were input into the software to ensure accuracy. The average volume percentage of the pores was found to be 38.2%, a number close to the theoretical 41.2%. The volume of pores (or the volume of the released Sn) in the bumps is approximately 63,879 μm^3. We assume that all of released Sn atoms have diffused to the side walls to form Cu_3Sn. This implies that 63,879 μm^3 of Sn would form 137,978 μm^3 of Cu_3Sn on the side walls. This is again close to the calculated value of 157,932 μm^3 for the volume of Cu_3Sn formed on the sidewalls in the actual bumps.

The above experimental results and calculation both indicate Sn diffusion to side walls of Cu UBM may be a possible mechanism for the formation of the porous Cu_3Sn. The porous Cu_3Sn will be a reliability issue for solder joints with Cu UBM. Yet, no solutions have been proposed so far to prevent it from happening. More studies need to be performed to solve this problem.

2.3 Conclusions

We have carried out a systematic study on an important reliability issue related to high-density packaging of microelectronic devices. In this study, SnAg solder bump samples with Cu UBM were stressed at current densities of 1.45×10^4 A/cm^2 and 1.20×10^4 A/cm^2, with operating temperatures of approximately 185 ^{o}C and 170 ^{o}C, respectively. A porous Cu_3Sn structure, unseen in traditional flip-chip solder joints, was observed in the process. Cu_3Sn IMCs were also observed on the side walls of Cu column UBM due to side wall reactions.

We have proposed a model to explain the formation mechanism of the observed porous Cu_3Sn and side-wall Cu_3Sn. In the reaction: $Cu_6Sn_5 \rightarrow Cu_3Sn + 3Sn$, one Cu_6Sn_5 molecule converted into three Cu_3Sn molecules and three Sn atoms were released. The released Sn left pores behind to form the porous Cu_3Sn. This is because when the early formed layer-type Cu_3Sn becomes a barrier to Cu diffusion, the released Sn atoms, taking an alternative path, diffuse to the side walls to form the Cu_3Sn IMCs by side wall reaction. Results of volume calculations were consistent with the proposed processes and consequently provided further evidence of this mechanism. A more detailed explanation will be presented in Chapter 4.

In the past, the layer-type Cu_3Sn is regarded as the terminal phase for the solid-state Cu-Sn reactions; however, our results conclude that the SnAg bump with low bump height would lead to porous-type Cu_3Sn formation when it is stressed with high current densities and high temperatures.

Chapter 3 Porous Cu_3Sn Formation by Solid State Aging

Intermetallic compounds (IMC) of Cu-Sn can be found in nearly all solder joints on Cu. The formation of Cu_6Sn_5 and Cu_3Sn during solid-liquid interdiffusion (SLID) bonding is essential in providing metallic bonds in a solder joint. On these two IMCs, the growth of Cu_6Sn_5 has been studied widely, whereas the growth of Cu_3Sn has received much less attention. This is because Cu_6Sn_5 is the first phase to form in the SLID or wetting reaction between molten solder and Cu. Even when the eutectic SnPb is replaced by the Pb-free SnAgCu, the first phase to form remains to be Cu_6Sn_5. Upon a longer reflow or a long time solid state aging, a layer-type Cu_3Sn will form between Cu_6Sn_5 and Cu.

However, in the recent trend of device minimization for mobile consumer electronic products, the size or thickness of solder joints is being reduced to 20 μm or less. In these microbumps, a new morphology of Cu_3Sn, the porous-type, has been found [24-27]. While the layer-type Cu_3Sn is known to contain Kirkendall voids [29-31], the porous Cu_3Sn has a much larger fraction of voids, near 40%. The porous Cu_3Sn does not form alone, and it co-exists with the layer-type Cu_3Sn. In this chapter, we analyze their competing growth. It is of interest from the point of view of reliability because the porous structure will have a very poor mechanical property.

3.1 Experimental

To design our test samples, we considered two extreme cases. First, if the solder thickness in the joint is large, such as 100 μm in a flip chip C-4 solder joint, no porous Cu_3Sn formation has been reported so far. Second, if the solder thickness is less than 10 μm, it can be transformed completely to a layer-type of Cu_3Sn, and no formation of porous Cu_3Sn. As a reference, we note that the thickness of Sn is only 3.6 μm in Ref. [24], which can be

transformed completely to a layer-type Cu_3Sn at 240 °C for 3 h as shown in Figure 3.5(d) in Ref. [24]. Upon further annealing at 24 and 96 h, no porous Cu_3Sn formation occurs. Combining these two considerations, we choose to use a microbump having a solder thickness about 20 μm.

In practice, a size around or less than 20 μm is particularly demanded for the application of 3D IC integration of chips containing TSVs. One of the primary reasons that the microbump having such size regime is because the diameter of TSV is also 20 μm or less. In order to interconnect multiple TSV-containing thinned chips in vertical direction, solder joint is to be scaled down to 20 μm.

Figure 3-1(a) is the schematic cross-sectional diagram of a solder joint with Cu column as under-bump-metallization (UBM) on both sides. The joint was made by joining an upper part and a lower part together. On the upper part, 1 μm Ti was sputtered as the adhesive layer on a Si chip. Then a layer of 2 μm Cu was sputtered as the seed layer for the subsequent electroplating of a column of 20 μm Cu as UBM. The diameter of the column was 30 μm. The composition and thickness of the solder layer was Sn-2.3Ag and 14 μm, respectively, and the deposition of the Sn was by electroplating. The layered structure on the lower part is the same as the upper part. The two parts (or two chips) were joined by solid-liquid interdiffusion (SLID) bonding by a reflow at 250 °C for few seconds with the use of a small amount of resin-based flux [38, 39]. Because this microbump sample was made one-by-one, rather than an array of them on large chips, underfill was used to enhance the mechanical strength of the joint in handling.

In this study, we have ignored the presence of 2.3% of Ag in the solder. Most likely, the Ag will form Ag_3Sn and it will be distributed in the microbumps. It does not seem to affect much of the layer-type and porous-type growth of Cu_3Sn.

Figure 3-1(b) shows SEM image of the cross-section of a microbump right after SLID. A layer of scallop-type Cu_6Sn_5 was found at the two interfaces on either side of the middle and unreacted solder. Then, a second reflow at 260 °C for 90 sec and followed by a solid state annealing at 200 ºC for 1 day was performed to transform the scallop-type Cu_6Sn_5 and the remaining solder into layer-type of Cu_3Sn and Cu_6Sn_5 between the Cu. We have a layered structure of $Cu/Cu_3Sn/Cu_6Sn_5/Cu_3Sn/Cu$, as shown in Fig. 3-1(c). The thickness of the Cu_3Sn is about 1.8 μm. We note that all the solder has been consumed. Also there is a thin layer of side-wall formation of Cu_3Sn. This is the beginning microstructure of our test samples for the subsequent annealing at 220 °C and 260 °C to study the growth competition of the layer-type and porous-type of Cu_3Sn.

Two sets of samples were annealed respectively at 220 ºC for 20, 50, 100, and 300 h and at 260 °C for 30, 90, 210, 300, 390, and 720 min. These annealed samples were cross-sectioned and polished for microstructure and composition examination with a JEOL 6500 field-emission scanning electron microscope (SEM) and energy dispersive spectroscopy (EDS).

To study the 3-dimensional porous morphology of Cu_3Sn, synchrotron radiation (SR) tomography using TXM facility [33] of beamline BL01B [34] at the National Synchrotron Radiation Research Center (NSRRC) in Taiwan was performed. Using software to cut various cross-sections of the 3-dimensional images of the porous structure, we were able to measure the thickness and distribution of lamellar voids and compare them to the 2-dimensional porous images obtained by SEM. In addition, we measured the fraction of total void volume in the porous microstructure and the interconnectivity of the voids.

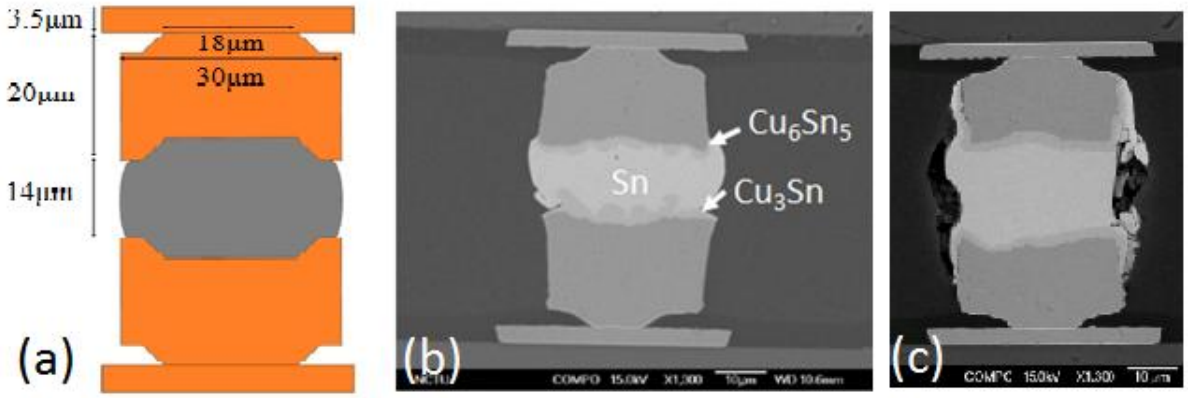

Figure 3-1 (a) Schematic diagram of the cross-section of a microbump, (b) SEM image of the cross-section of a microbump after SLID bonding, and (c) SEM image of the cross-section of an as-fabricated microbump, which is the beginning microstructure for subsequent annealing at 220 °C and 260 °C.

3.2 Results

Figure 3-2 shows a set of SEM cross-sectional images of the samples after various annealing time at 220 °C. Figure 3-2(a) is the image of a sample annealed for 20 h. A symmetrical layered structure of Cu/Cu_3Sn/Cu_6Sn_5/Cu_3Sn/Cu is seen, but no formation of porous Cu_3Sn. The thickness of Cu_3Sn and Cu_6Sn_5 layers are 3.5 μm and 14.6 μm, respectively. However, we note that there is already a thick side-wall formation of Cu_3Sn. The side-wall formation here is unrelated to porous Cu_3Sn formation. Figure 3-2(b) is the image of a sample annealed for 50 h, and the thickness of Cu_3Sn and Cu_6Sn_5 layers has changed to 6.5 μm and 11.5 μm, respectively.

The measurement of thickness has an uncertainty of about ± 0.5 μm. We notice that when the thickness of Cu_3Sn reaches about 6.5 μm on either side, it will not grow much thicker upon further annealing. This is because it is diffusion-controlled, the growth will slow

down when the layer of Cu_3Sn becomes a diffusion barrier to its own growth. On the other hand, if porous Cu_3Sn forms, the competing growth will reduce the growth of the layer-type Cu_3Sn strongly.

Figure 3-2(c) shows the image of a sample annealed for 100 h. We note that the porous Cu_3Sn begins to form at the circumference of the middle Cu_6Sn_5 layer. The lateral growth of the porous Cu_3Sn is in the radial direction, going from the edge towards the center. Figure 3-2(d) shows the image of a sample annealed for 300 h, wherein the middle layer of Cu_6Sn_5 has transformed completely into porous Cu_3Sn. We obtain a layer of porous Cu_3Sn sandwiched between two layer-type of Cu_3Sn. The interface between the porous and the layered Cu_3Sn is unique and not much is known about it.

Accompanying the porous-Cu_3Sn formation, a thick side-wall formation of Cu_3Sn is found. However, the growth of side-wall Cu_3Sn has increased as compared to that in Figures 3-2(a) and 3-2(b), but the increase is not substantial. Also some damage occurs in the underfill surrounding the microbump. The damage could be due to the reaction between the underfill and Cu_6Sn_5, which dissolved some Sn from the Cu_6Sn_5 and affected the formation of the porous Cu_3Sn. At 1000 hours, the layer type Cu_3Sn had completely consumed the copper UBM and the porous Cu_3Sn at the center had shrunk, as shown in Figure 3-2(e). This morphological change of Cu_3Sn, from the porous type to layered type, is the result of extended annealing.

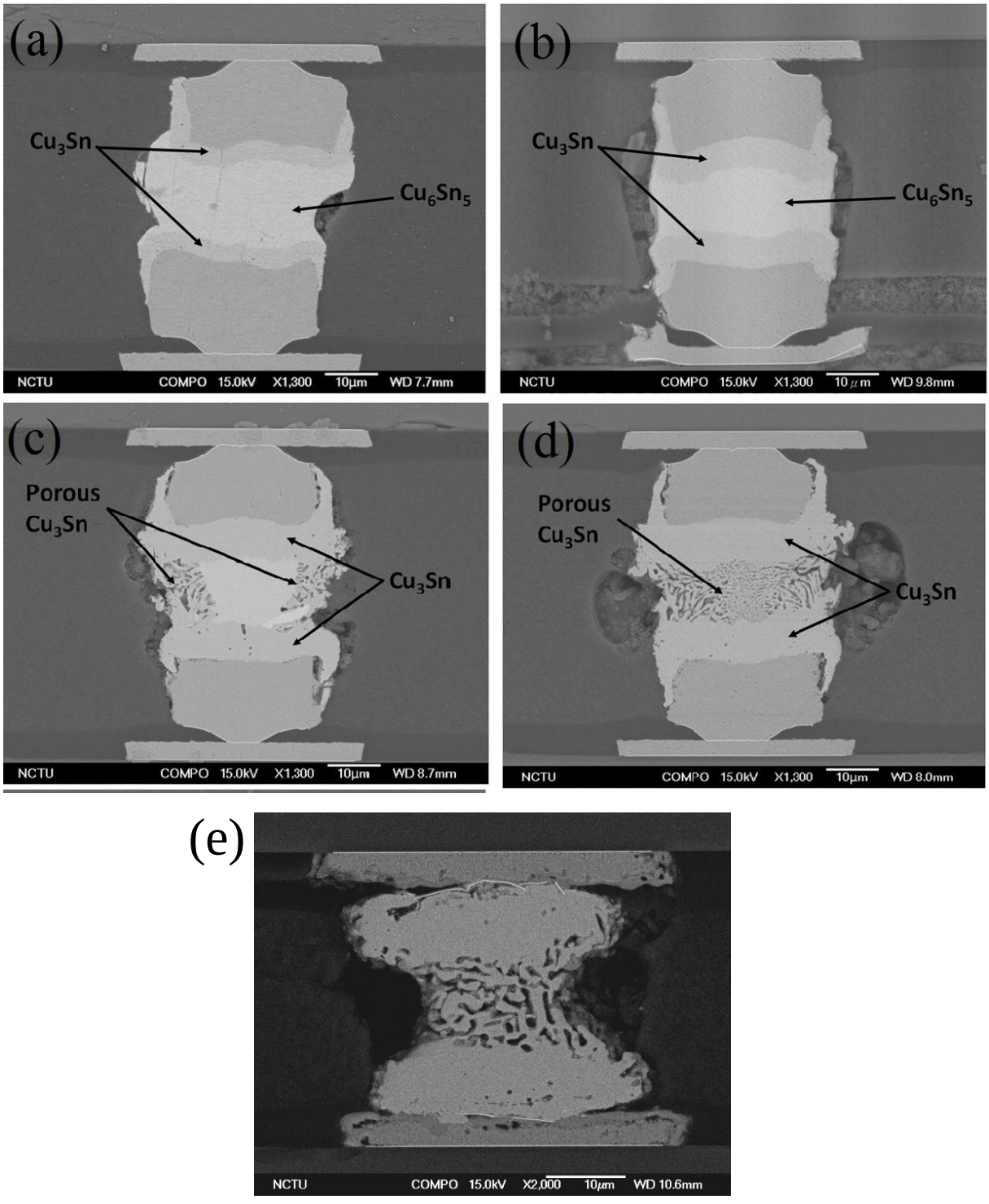

Figure 3-2 SEM image of the cross-section of microbumps annealed at 220 °C.

(a) 20 hours, (b) 50 hours, (c) 100 hours, (d) 300 hours, and (e) 1000 hours.

Figure 3-3 shows a set of SEM cross-sectional images of samples after various annealing at 260 ºC. Figures 3-3(a) and 3-3(b) are respectively the images after 30 and 90 min. Both layer-type and side-wall formation of Cu_3Sn are seen, yet there is no porous Cu_3Sn formation. The measured thickness of the layer-type Cu_3Sn is shown in Table 1. Figures 3-3(c) and 3-3(d) are, respectively, the images after 210 and 300 min. We find a small amount of porous Cu_3Sn formation at the corner of circumference of Cu_6Sn_5. Figures 3-3(e) and 3-3(f) are, respectively, the images after 390 and 720 min. The formation of porous Cu_3Sn is clear and in Figure 3-3(f) the transformation of Cu_6Sn_5 to porous Cu_3Sn is completed, which is similar to Figure 3-2(d). Both types of Cu_3Sn co-exist; their growth competition will be studied below.

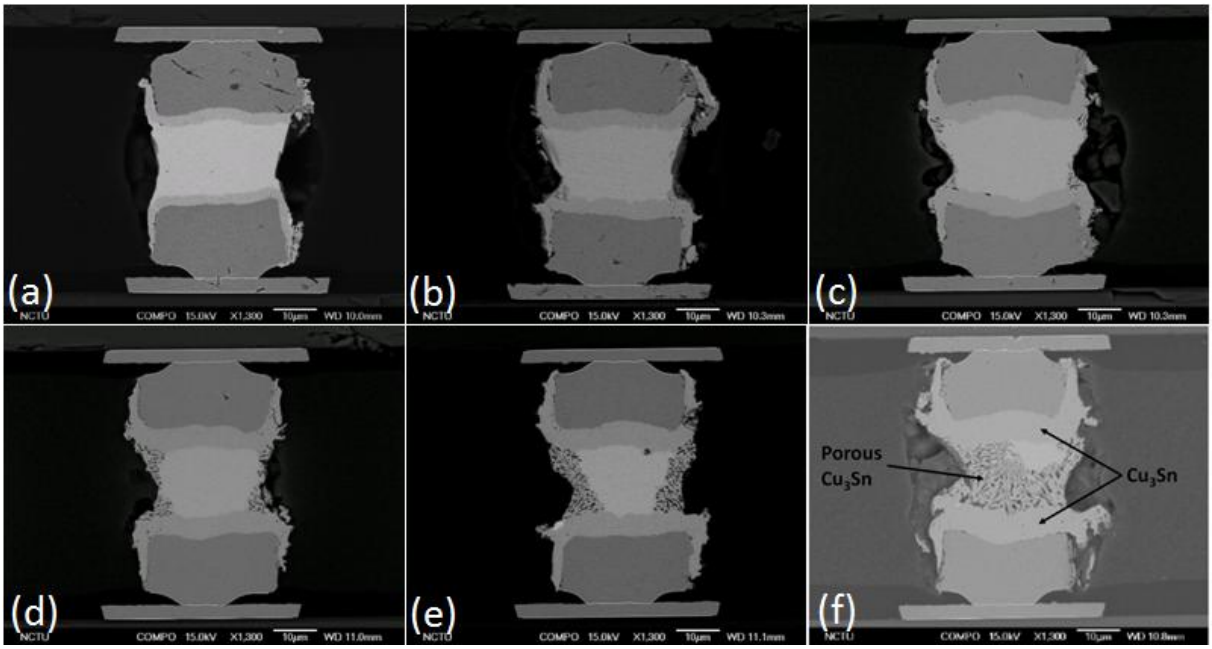

Figure 3-3 SEM image of the cross-section of microbumps annealed at 260 °C.
(a) 30 min, (b) 90 min, (c) 210 min, (d) 300 min, and (e) 390 min (f) 720 min.

Table 1 lists the raw data of thickness of the layer-type Cu_3Sn against time as measured form Figures 3-2 and 3-3. To plot them, we note that since there is already an initial thickness

of 1.8 μm of Cu_3Sn, we should either subtract the thickness or add a time. The time is an estimate time needed to grow a layer of 1.8 μm Cu_3Sn at 220 °C and at 260 °C, respectively. Because it is a diffusion-controlled growth, it should follow the random walk relation of $x^2 = Dt$, which means that it is easier to add time. However, adding a constant time in plotting the curve is to displace the entire curve slightly to the right, provided that we take the *x*-axis as time as shown in Figure 3-4. Therefore, we just plot the raw data in Figure 3-4.

Table 1
Data of Cu_3Sn layer thickness vs. time.

220 °C		
Time (hr)	Thickness (μm)	Thickness^2
20	3.51	12.32
50	5.88	34.57
100	7.01	49.14
300	8.24	67.89
260 °C (from Fig. 2)		
Time (min)	Thickness (μm)	Thickness^2
30	2.41	5.80
150	3.62	13.10
210	3.95	15.60
300	4.7	22.09
390	5.22	27.24
720	6.58	43.29

Figures 3-4(a) and 3-4(b) are, respectively, plots of the thickness and the square of thickness of Cu_3Sn as a function of annealing time at 220 °C. Figure 3-4(c) and 3-4(d) are similar plots for the annealing at 260 °C. In Figure 3-4(a), we see the growth slows down greatly with time. In Figure 3-4(b), we should expect a straight line indicating a diffusion-control growth. However, except the early period, the growth drops down with annealing. We note that when the layered growth slows down, the beginning of growth of the porous Cu_3Sn occurs. While the growth of the layered-type slows down, it still grows, so we have the co-existing and competing growth of both types. At the same time, there are side-wall reactions

to form a layer of Cu_3Sn on the Cu bumps. Comparing Figures 3-3(a) and 3-3(b) to Figures 3-3(c) and 3-3(d), we find that the latter has had more side-wall growth than the former.

At 260 °C, Figure 3-4(c) shows a slowing down of growth with time, and Figure 3-4(b) shows a straight line plot of square of thickness against time, which is expected. However, we note that in Figure 3-4(b), the layer-type growth does not slow down much when the porous growth occurs, which is quite different from that in Figure 3-3(b). It might suggest that there was no competing growth between the layer-type and porous-type of Cu_3Sn, in Figure 3-3. We will examine this point later when we discuss the interface between them.

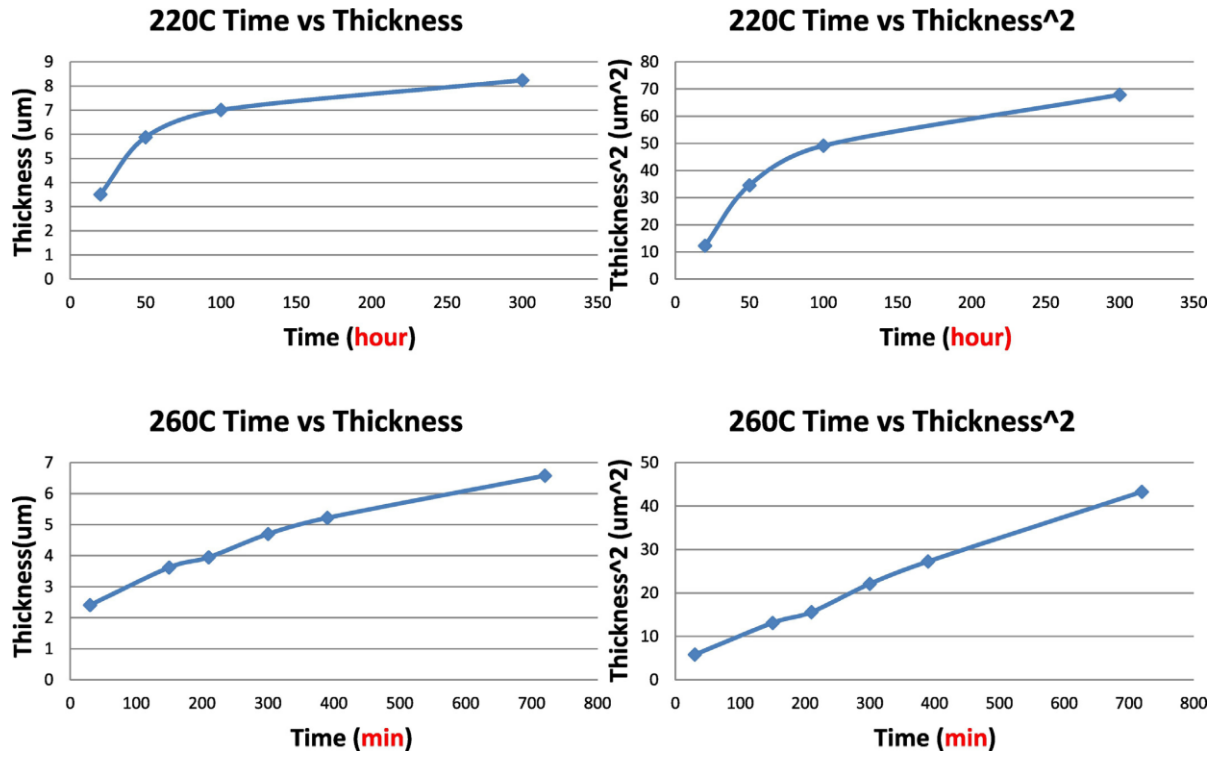

Figure 3-4 (a) Plot of layer thickness of Cu_3Sn against time at 220 °C, (b) Plot of square of layer thickness of Cu_3Sn against time at 220 °C, (c) Plot of layer thickness of Cu_3Sn against time at 260°C, and (d) Plot of square of layer thickness of Cu_3Sn against time at 260 °C.

Figure 3-5 shows a set of SR tomography images of the porous structure of Cu_3Sn. Figures 3-5(a) to 3-5(c) show the 3-D tomography of the porous structure inside Cu_3Sn with inverse signal contrast. Bright regions reveal the 3-D distribution of the porous structure. Figures 3-5(d) to 3-5(f) show thin sections obtained from the 3-D tomography of the porous Cu_3Sn. Here, the dark regions reveal the 2-D distribution of the porous structure. The thickness of each section is about 250 nm. Each section is obtained with a 500 nm relative distance inside the Cu_3Sn.

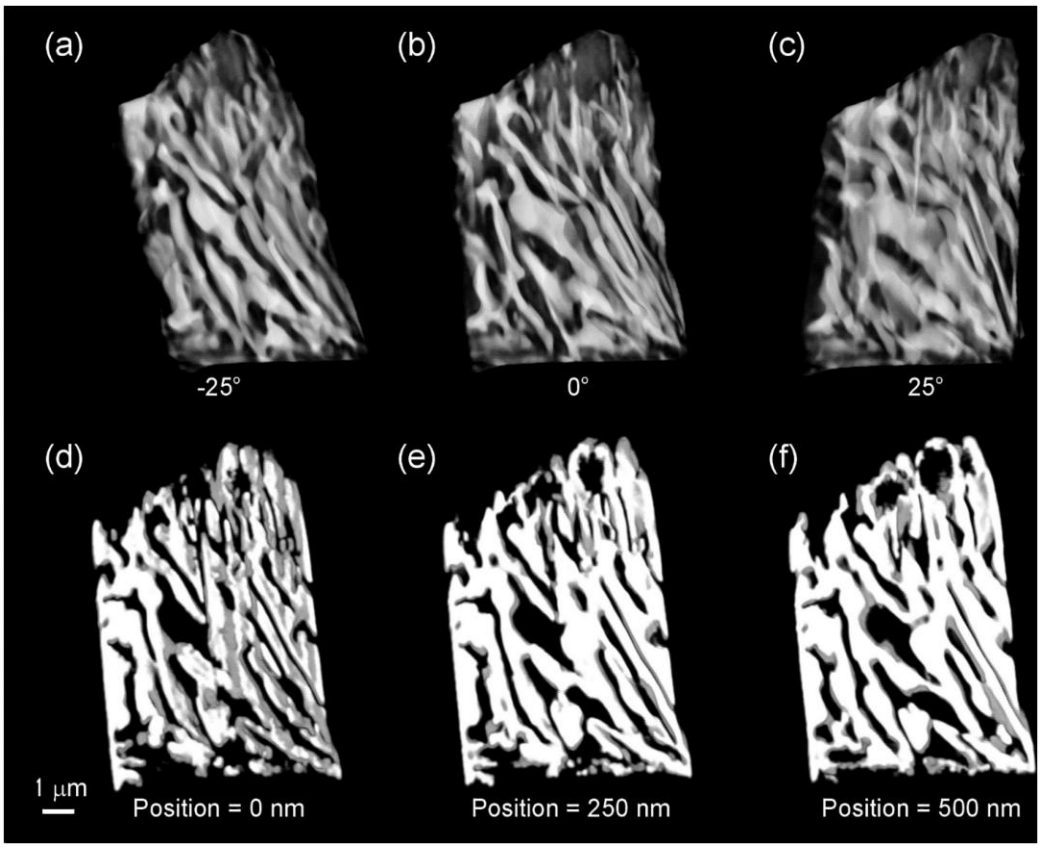

Figure 3-5 Synchrotron radiation tomography. (a) to (c) show the 3-D tomography of the porous structure inside Cu3Sn with inverse signal contrast. Bright regions reveal the 3-D distribution of the porous structure. (d) to (f) show thin sections obtained from the 3-D tomography of the porous Cu_3Sn. Here, the dark regions reveal the 2-D distribution of the porous structure.

What we have learned from the SR tomography images are given below. First, the porous structures are interconnected, rather than isolated. The interconnected lamellar pores provide a continuous path for the out-diffusion of Sn. The width of the lamellar pores can be measured to be about 1 μm, which can also be measured from the 2D SEM images in Figure 3-2. Second, the total void volume can be estimated to be around 40%, which is in close agreement with the theoretical calculation of volume change from solid Cu_6Sn_5 to porous Cu_3Sn. We should point out that at present the SR images do not have the resolution to offer a precise measurement of the actual volume fraction. The uncertainty is because of the software used in the tomography image analysis. We further note that, in this study, a set of only the top die were tested.

3.3 DISCUSSIONS

3.3.1 The Transformation of Cu_6Sn_5 to Cu_3Sn in a Microbump

In the binary phase diagram of Cu-Sn, the phase of Cu_3Sn is between Cu_6Sn_5 and Cu. Therefore, Cu can be at equilibrium withCu_3Sn, but not with Cu_6Sn_5. In a microbump with thick Cu UBM, while Cu_6Sn_5 forms first, it is unstable because of the excess Cu and has to transform to Cu_3Sn. Whether it transforms to a layer-type or a porous-type Cu_3Sn will be discussed below. Nevertheless, the porous-type structure has a much larger area of surfaces, in turn a much higher energy, than the layer-type structure, so the latter should form first. Only when the Cu_6Sn_5 cannot be transformed fast enough by the growth of the layer-type Cu_3Sn, the porous-type Cu_3Sn will join.

3.3.2 Formation of Layer-Type Cu_3Sn but no Formation of Porous-Type Cu_3Sn

We recall that the ball-grid-array (BGA) solder joints have a diameter of 760 μm, and the C-4 flip chip solder joints have a diameter of 100 μm. In these joints, even if they have had a

solid state aging at 150 °C for 1000 h, the thickness of layer-type of Cu_6Sn_5 and Cu_3Sn can be about 10 μm. However, no porous Cu_3Sn formation has been reported in them, because there is plenty of free or un-reacted Sn in them. The formation of porous Cu_3Sn comes from the depletion of Sn from Cu_6Sn_5, and if there is un-reacted Sn around, it is no need to deplete Sn from Cu_6Sn_5, in turn no porous Cu_3Sn formation.

On the other hand, when the initial thickness of solder in the joint is below 10 μm, it is insufficient to form both the Cu_3Sn and the Cu_6Sn_5 in thick layers, even if there is a thick UBM of Cu. The entire 10 μm solder can be reacted to form a single layer of Cu_3Sn, without Cu_6Sn_5, as reported in Ref. [24] The porous Cu_3Sn cannot form simply because there is no Cu_6Sn_5 for decomposition.

Even if there is Cu_6Sn_5 for decomposition, the depleted Sn must find a sink. It has been shown that the soldering flux can have a solubility of Sn [24]. Therefore, the flux as well as the side-wall of Cu UBM can be a sink for Sn, which has been reported in Ref. [24]. If we can clean the flux and if we can prevent side-wall reaction from taking place, the chance of porous Cu_3Sn formation will be greatly reduced.

3.3.3 Growth Competition between the Layer-Type and Porous-Type of Cu_3Sn

For the formation of porous Cu_3Sn, it helps to have a critical thickness of the layer-type Cu_3Sn. To appreciate this point, we assume a competing growth between the porous-type Cu_3Sn and the layer-type Cu_3Sn. When the latter is thin, its diffusion-control growth is fast, and the chance for the former to form is slim. But, when the layer-type becomes very thick and its growth slows down significantly, the porous-type can grow.

We consider the following two chemical formulae of the additive and subtractive reaction respectively in converting Cu_6Sn_5 to Cu_3Sn,

$$Cu_6Sn_5 + 9Cu \rightarrow 5Cu_3Sn \quad (5)$$

$$Cu_6Sn_5 - 3Sn \rightarrow 2Cu_3Sn \quad (6)$$

The first equation favors the reaction to form Cu_3Sn by adding Cu, and it occurs in the growth of the layer-type Cu_3Sn. The second equation favors the reaction to form Cu_3Sn by subtracting Sn, and it occurs in the growth of porous Cu_3Sn. In principle, either one of them can be independent of the other. Experimentally, they seem to be coupled and in competition. Both equations show that Cu_6Sn_5 alone will not decompose into Cu_3Sn and Sn. This is supported by the fact that if we take a bulk piece of Cu_6Sn_5 and anneal it, it is stable and no decomposition occurs.

In order to add Cu to the reaction in Eq. (5), Cu is available from the thick Cu UBM in a microbump. To take Sn away from Cu_6Sn_5 in Eq. (6), there must be a sink for Sn. In a microbump, the nearby Cu surface of the Cu UBM can do so. Thus, we need a third equation as below,

$$3Sn + 9Cu \rightarrow 3Cu_3Sn \quad (7)$$

Equation (7) means that Sn goes to a Cu sink to form Cu_3Sn. Physically, we have found that Sn can go to the side-wall of Cu column to form Cu_3Sn. If we add Eqs. (6) and (7), we obtain Eq. (5). Thus, thermodynamically we have the same transformation of Cu_6Sn_5 to Cu_3Sn in Eq. (5) as well as in Eq. (6) plus Eq. (7), and this is the reason why they can be independent, except that the morphology and kinetic paths are different.

In Eq. (5), the growth of the layer-type Cu_3Sn occurs by the diffusion of Cu from the Cu UBM across the layer-type Cu_3Sn to react with Cu_6Sn_5. In Eqs. (6) and (7), the growth of Cu_3Sn occurs in two locations; the first location is the porous-type Cu_3Sn which is

sandwiched between two layer-type of Cu_3Sn, and the second location is a thin coating layer of Cu_3Sn on the side-wall of Cu column.

Therefore, both Eq. (5) and Eq. (6) require the presence of Cu in order to allow the reactions to proceed. Their competition depends on the supply and the location of Cu. When the supply of Cu across Cu_3Sn from the Cu UBM is rapid and abundant, the reaction in the first equation is dominant. If not, the reaction in the second equation may occur when the side-wall of Cu column serves as the sink for Sn, then porous Cu_3Sn forms. In their competition, the layer-type wins when it is thin with a fast growth rate. When it slows down, the porous-type begins to grow, provided that there is a sink for Sn.

However, there is an interesting question on the porous structure formation. How come the diffusion of 9 Cu atoms as shown in Eq. (5) only leads to some Kirkendall voids formation but no porous structure formation? Yet why does the diffusion of 3 Sn atoms in Eq. (6) lead to porous structure formation with about 40% of void volume? We will explain the difference in Section 3.3.5, where the issue of lattice shift will be discussed.

Whether the reaction temperature is above or below the melting point of Sn (232 °C) or the Pb-free solder (slightly below 217 °C) seems less important, nevertheless the rate of porous Cu_3Sn formation is affected as shown in Figure 3-2(d) and Figure 3-3(f). This has also been observed in Ref. [24]. But the temperature cannot be too low, say below 170 ^oC, no porous structure of Cu_3Sn has been found here when the sink is the side-wall of Cu. On the other hand, if soldering flux is the sink of Sn, we expect the porous Cu_3Sn can be formed at a lower temperature due to chemical etching.

3.3.4 The Interface between the Porous-Type and the Layer-Type Cu_3Sn

Across the interface, there is no change in composition, but a change in microstructure and crystallographic orientation. It is not a conventional grain boundary because the porous side has a much higher energy due to a very large area of void surface. The energy difference is much more than Gibbs-Thomson effect of grain boundary curvature. Therefore, the interface is intrinsically unstable; the layer-side will grow and consume the porous-side in order to remove the void surfaces, provided that temperature is high enough for it to occur. This seems to have taken place in the 260 °C annealing. This is a direct growth competition, wherein the layer-type consumes the porous-type, as shown in Fig. 3-2(e).

We note that during the 220 °C and 260 °C annealing, the growth direction of the layer-type is normal to the interface, but the porous-type is parallel to the interface. We expect to see a tapered interface, yet the interfaces as shown in Figures 3-2 and 3-3 are rather horizontal, which may mean that during the competition, the layer-type is dominant. Indeed, a much longer annealing at 260 °C will give us more information.

3.3.5 Lattice Shift and Its Amount to be Measured by Synchrotron Radiation Tomography

Lattice shift means whether the vacant sites left behind by the out-diffusion of Sn, can be absorbed by the IMC lattice or not. Complete or incomplete lattice shift means all or a part of the vacancies are absorbed. We recall that in Darken's analyze of Kirkendall effect in interdiffusion [40], an important assumption is that vacancy is at equilibrium everywhere in the diffusion couple, so lattice shift (as revealed by the marker motion) is complete, and as a consequence no void formation occurs in Darken's analysis. However, experimentally, Kirkendall voids (or Frenkel voids) can form because of incomplete lattice shift [29-31]. This is the major difference between Kirkendall void formation (lattice shift occurs) in the layer-

type growth and the lamellar pores formation in porous-type growth (no or very little lattice shift occurs) of Cu_3Sn.

To determine the amount of lattice shift in porous Cu_3Sn formation, we need an accurate measurement of the total volume in the porous structure. If the total volume matches the calculated value of 40.9%, it means no lattice shift. Experimentally, we do expect a small amount of lattice shift or a small amount of vacancies to be absorbed by the IMC lattice. As we have pointed out that in order to provide a multiple and continuous diffusion paths for Sn to diffuse out, only a small amount of lattice shift is allowed and the amount may depend on the annealing temperature. This means that synchrotron radiation tomography measurement of the total volume is of fundamental interest in understanding the porous phase formation.

3.3.6 The Link between Side-Wall Formation and Porous Formation of Cu_3Sn

In Figures 3-1(c), 3-2(a), and 3-3(a), we have observed side-wall formation of Cu_3Sn without the formation of porous Cu_3Sn. It indicates that there is no direct link between side-wall formation and porous formation. However, we have assumed that side-wall formation can serve as the sink of Sn during the porous Cu_3Sn formation. We have explained that the formation of lamellar type of void in the porous structure is because of the absence of vacancy absorption by the IMC lattice during the out-diffusion of Sn. Then, in the side-wall reactions in Figures 3-1(c), 3-2(a), and 3-3(a), the question is what has happened to those vacancies with the Sn diffusion.

Actually, accompanying the side-wall formation, a neck or groove forms around the circumference of Cu_6Sn_5. The layer of Cu_6Sn_5 has the shape of a pulley, see Figures 3-2(a) and 3-3(c). It is due to the surface diffusion of Sn and the condensation of vacancies to form the groove on the circumference of the layer-type Cu_6Sn_5. In the literature, side-wall reaction

has been reported [16]. The critical link between lattice shift and lamellar porous structure is that if a substantial amount of lattice shift occurs, the formation of the continuous and interconnecting voids will be blocked.

3.4 Conclusions

Experimental studies of chemical reactions in solder microbumps have found growth competition between the porous-type and layer-type of Cu_3Sn. In the latter, we assume that Cu is the dominant diffusing species and it reacts with Cu_6Sn_5 to grow the layer-type Cu_3Sn. In the former, we assume that Sn is the dominant diffusing species. The Sn is depleted from Cu_6Sn_5 and is driven to the side-wall of Cu column in the microbump to form a coating of Cu_3Sn. The depleted Cu_6Sn_5 transforms to porous Cu_3Sn. The growth competition has been analyzed. Synchrotron radiation tomography has been used to measure the volume fraction (to be near 40%), and the interconnected distribution of lamellar-type of voids in the porous Cu_3Sn.

Chapter 4 Formation Mechanism of Porous Cu_3Sn

Intermetallic compounds of Cu-Sn can be found in nearly all solder joints and it becomes even more important in microbump for 3D IC application. The formation of Cu_6Sn_5 and Cu_3Sn is essential in providing the metallic bonding between Cu and solder. Of these two Cu-Sn IMCs, the growth of Cu_6Sn_5 has been investigated widely, while the understanding of kinetics, failure mechanism and reliabilities of Cu_3Sn is still on-going and relatively immature. In a recent publication [27], it has considered in considerable details the formation mechanism of porous Cu_3Sn, on which this chapter is based.

4.1 Review of Experimental Observations

We begin with a brief discussion on the experimental situation wherein the layer-type Cu_3Sn formation has been found, but no porous Cu_3Sn formation was observed, as shown in Figures 3-2(a) and 3-2(b). Ball-grid-array (BGA) solder joints have a diameter of 760 μm, and flip chip solder joints have a diameter of 100 μm. Both have typically a thin UBM of Cu of several μm. In these joints, the total thickness of Cu_6Sn_5 and Cu_3Sn can be close to 10 μm, even if the joints have had a long solid state aging at 150 °C for 1000 h. The Cu_3Sn has layer-type morphology, yet no porous Cu_3Sn formation has been reported in BGA and flip chip solder joints. As discussed in Chapter 3, the reason is in these large size solder joints, there is plenty of free or un-reacted Sn. Because the formation of porous Cu_3Sn comes from the depletion of Sn from Cu_6Sn_5, if there is un-reacted Sn around, it is no need to deplete Sn from Cu_6Sn_5, in turn no porous Cu_3Sn formation. When the initial thickness of solder in the joint is thin, below 10 μm, it is insufficient to form both Cu_3Sn and Cu_6Sn_5 in thick layers. The porous Cu_3Sn cannot form simply because there is little Cu_6Sn_5 for decomposition.

Yet, when the initial solder thickness is about 20 to 50 μm in a microbump, the solder can be reacted completely to form a thick layer-type structure of $Cu/Cu_3Sn/Cu_6Sn_5/Cu_3Sn/Cu$. In it, when the growth of the Cu_3Sn layers reaches about 10 μm thick, the Cu_3Sn gradually becomes a diffusion barrier for Cu to diffuse across it to react with Cu_6Sn_5, so the growth of the layer-type Cu_3Sn slows down greatly. Consequently, the middle layer of Cu_6Sn_5 remains. However, Cu_6Sn_5 is unstable with Cu, but Cu_3Sn is stable with Cu. If there is free Cu in the system, Cu_6Sn_5 tends to decompose. It can occur by two ways; either adds Cu to Cu_6Sn_5 or subtracts Sn from Cu_6Sn_5.

The side wall of Cu serves as the free Cu to attract Sn, provided that the free surface is not covered by oxide, so the effect of solder flux is important [24]. Side wall reaction with Sn has been found to play a significant role in porous Cu_3Sn formation [26]. This is because the side wall of Cu serves as a sink for the Sn depleted from Cu_6Sn_5. If we can prevent side wall reaction from taking place, the chance of porous Cu_3Sn formation will be greatly reduced.

We discuss the mechanisms related to these observations in details below.

4.2 The Necessary and Sufficient Conditions for Porous Cu_3Sn Formation

Below, we postulate the necessary and sufficient conditions for porous Cu_3Sn formation.

(1) There is a critical layer thickness of Cu_3Sn in the multilayer-type reaction of $Cu/Cu_3Sn/Cu_6Sn_5$. Below the critical thickness, the growth of the layer-type Cu_3Sn is dominant. Above it, the formation of porous Cu_3Sn can occur. This is because when the Cu_3Sn is thicker than the critical thickness, it becomes a diffusion barrier to Cu. The critical thickness is found experimentally to be about 5 to 10 μm, depending on the temperature of reaction. Kirkendall void formation in Cu_3Sn may have a blocking effect on Cu diffusion, and in turn it may affect the critical thickness.

(2) It requires no free Sn or un-reacted Sn in the solder joint. For this condition, no porous

Cu_3Sn has been reported in large BGA and flip chip solder joints, where the un-reacted Sn is abundant.

(3) There exists a nearby sink for Sn. The out-diffusion of Sn from Cu_6Sn_5 leads to the decomposition of Cu_6Sn_5. When the Cu_6Sn_5 is depleted of Sn, it forms porous Cu_3Sn. It starts from the circumference of the Cu_6Sn_5 and grows towards the center of the microbump along the radial direction.

(4) The reaction temperature must be high enough for the decomposition of Cu_6Sn_5 to occur and for the diffusion of Sn to reach the sink. Experimentally it is found that porous Cu_3Sn does not form below 170 °C. Whether the reaction temperature is above or below the melting point of pure Sn or the Pb-free solder seems unimportant for porous Cu_3Sn formation, nevertheless it affects the rate of porous Cu_3Sn formation.

(5) The vacant sites left behind by the Sn flux will form huge voids, and they could block the Sn flux and stop the porous Cu_3Sn formation. To prevent the voids from blocking the diffusional flux of Sn, a lamellar type porous structure is chosen. During the out-diffusion of Sn, the vacant sites left behind are not absorbed by the Cu_3Sn lattice, which means no lattice shift. Furthermore, in the porous-type lamellar structure, having a set of the lamellae as voids, it enables a high rate of formation of the porous structure. More importantly, the void volume fraction is about 40%, which shows that the depletion of Sn can be complete as calculated by using Eq. (6). It is worth mentioning that in classical cellular precipitation in a closed system, the lamellar precipitation is incomplete (as will be discussed in Sec. 5.1).

4.3 Lattice Shift in the Growth of Layer-Type Cu_3Sn

Figure 4-1 is a flowchart of the formation of porous Cu_3Sn. In Figure 4-2, we depict the cross-section of a 3-layered structure of $Cu/Cu_3Sn/Cu_6Sn_5$. Upon annealing at temperatures around 200 to 300 °C, the middle layer of Cu_3Sn will grow at the expense of Cu and Cu_6Sn_5 according to Eq. (5). At the interface x_1 between Cu and Cu_3Sn, we assume that there is no chemical reaction except the diffusion of Cu into Cu_3Sn. This is because Cu_3Sn is the equilibrium phase on Cu, according to the binary phase diagram of Cu-Sn. Actually there is a small concentration range of Cu_3Sn in solid state and it facilitates the dissolution and diffusion of Cu into Cu_3Sn. However, the driving force of Cu diffusion in Cu_3Sn is not the small concentration gradient in Cu_3Sn, but it is the chemical potential gradient owing to the gain in IMC formation energy.

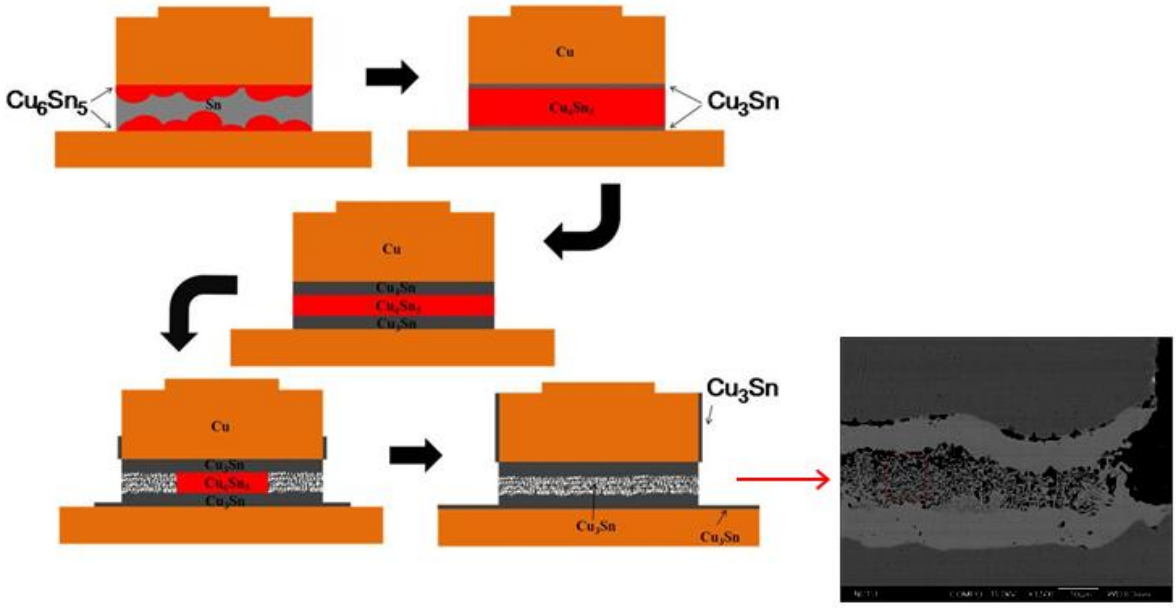

Figure 4-1 Flowchart of the formation of porous Cu_3Sn.

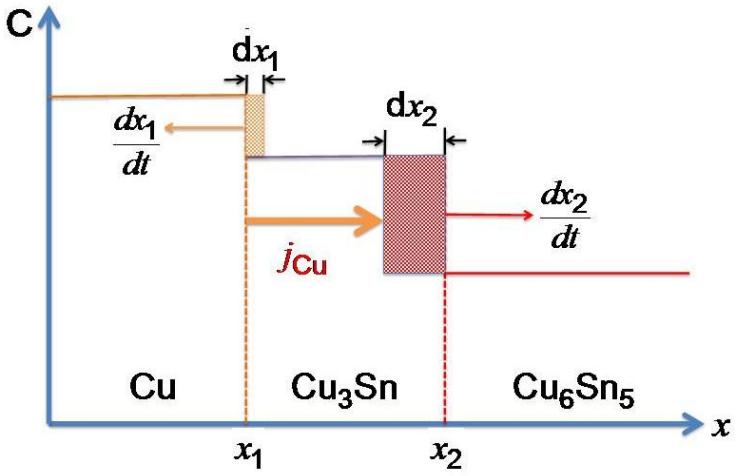

Figure 4-2 Schematic diagram of the growth of Cu_3Sn between Cu and Cu_6Sn_5.

Due to the dissolution and diffusion, we assume that in a time interval of dt, the interface of x_1 moves (to the left) into Cu by dx_1. Consider a unit area on the interface, depicted by the growth of the smaller shaded area in Figure 4-2, we can regard $dx_1 \cdot 1$ to be the volume of consideration. Within this volume the number of Cu atoms is given by $Cdx_1 \cdot 1$, where C is the number of Cu atoms per unit volume. We note that for pure Cu, we have $C\Omega = 1$, where Ω is the atomic volume of Cu ($\Omega = a^3/4 = 1/18\times10^{-29}$ m^3, where a = 0.3615 nm is the lattice parameter of Cu). These Cu atoms form the flux of Cu (j_{Cu}) diffusing into Cu_3Sn, and we have (by dropping the unit area),

$$\frac{dx_1}{dt} = -\frac{j_{Cu}}{C} = -j_{Cu}\Omega \qquad (8)$$

Accompanying this flux, the interface x_1 is advancing into Cu, as shown in Figure 4-2. At the same time, the entire lattice of Cu_3Sn is moving to the left together with x_1. This is defined

as “lattice shift” in interdiffusion. When the shift is 100%, no Kirkendall void will form. However, in most cases, there is some Kirkendall void formation. In Eq. (8), we have assumed that the shift is 100%. Thus the lattice shift explains why the Cu diffusion does not lead to porous structure formation, or it explains why Kirkendall void formation cannot explain the porous Cu_3Sn formation. The latter requires no lattice shift.

The flux of Cu in Eq. (8) will diffuse across the Cu_3Sn and react with Cu_6Sn_5 at the interface of x_2. The interface at x_2 will move (to the right) a distance of dx_2 into Cu_6Sn_5 due to reaction in Eq. (5) to form 5 molecules of Cu_3Sn, as depicted by the larger shaded area in Figure 4-2. However, for the motion of x_2, we must take into account the lattice shift at the interface x_1, or the motion of the interface at x_1.

In the volume of $dx_2 \cdot 1$, we take into account only the growth of 5 Cu_3Sn as shown by Eq. (5), we disregard the in-diffusion of 9 Cu atoms nor the consumption of one molecule of Cu_6Sn_5. This is because we consider here only the growth of Cu_3Sn. Therefore, for one Cu atom diffuses into the volume of $dx_2 \cdot 1$, it leads to the formation of 5/9 of one molecule Cu_3Sn. Now if we take the volume of one molecule of Cu_3Sn as V, we simplify it by assuming that $V \approx 4\Omega$. We have the following equation by the conservation of volume.

$$j_{Cu}\frac{5}{9}Vdt = dx_2 - dx_1$$

$$\frac{dx_2}{dt} = j_{Cu}(\frac{5}{9}V - \Omega) = j_{Cu}\frac{11}{9}\Omega \qquad (9)$$

Comparing Eq. (8) to Eq. (9), we see that the interface at x_2 is moving slightly faster than the interface at x_1, in opposite direction. It is worth mentioning that we do not consider lattice shift of the interface at x_2. This is because we assume that there is no flux of Sn diffusing from

x_2 into Cu_3Sn. Theoretically and experimentally, there should be some because there is a concentration gradient of Sn, nevertheless we have ignored it in the above analysis.

For the growth of a layer-type of Cu_3Sn by taking the sum of Eq. (8) and Eq. (9), we can obtain a diffusion-controlled growth,

$$W^2 = 4\tilde{D}t \qquad (10)$$

where W is the width of the Cu_3Sn layer and $\tilde{D}$ is interdiffusion coefficient in Cu_3Sn. Experimentally, the width of the layer can be measured as a function of time and temperature, so $\tilde{D}$ can be determined and in turn its activation energy. This is well known.

4.4 No Lattice Shift and Thermal Stability of Porous Cu_3Sn

The distribution of pores in the porous Cu_3Sn is periodic in lamellar shape, so the lamellar pores having a high density of surfaces. This is because of kinetic reason that it enables rapid surface diffusion of Sn, so the rate of porous Cu_3Sn formation is fast kinetically. No doubt, during the out-diffusion of Sn, there is atomic and lattice redistribution from Cu_6Sn_5 to Cu_3Sn. From the point of view of porous structure formation, the vacant sites left behind by the Sn atoms are not absorbed by the Cu_3Sn lattice, so there is no lattice shift and the vacant sites join to form the lamellar type of voids. Kinetic analysis of porous Cu_3Sn formation in an open system has been published elsewhere [41]. It will not be repeated here, nevertheless it is quite different from the classic cellular precipitation in a closed system. The latter is an incomplete precipitation. In the open system, the lamellar precipitation is complete.

However, the lamellar voids are intrinsically unstable, they tend to transform into circular voids, and then larger voids will form due to ripening.

4.5 Cu to be the Dominant Diffusing Species in Cu_3Sn

In the above kinetic analysis of layer-type of Cu_3Sn, we have assumed that Cu is the dominant diffusing species. It is a reasonable assumption because of the crystal structure of Cu_3Sn and the known Kirkendall effect [31]. In the orthorhombic crystal structure of Cu_3Sn, the sub-lattice of Cu enables the diffusion of Cu atoms without much of the resistance from a strong chemical effect in breaking Cu-Sn bonds. On the other hand, the diffusion of a Sn atom in Cu_3Sn must involve the breaking of a large number of Cu-Sn bonds. It means the diffusion of Cu is faster than that of Sn in Cu_3Sn. Furthermore, Kirkendall voids are found in Cu_3Sn and near the interface between Cu and Cu_3Sn.The formation of these Kirkendall voids has been explained by the decomposition of Cu_6Sn_5 into $2Cu_3Sn + 3Sn$, in which 9 Cu atoms will be added in order to react with the 3 Sn to form $3Cu_3Sn$. Some of the vacancies needed for the Cu diffusion may nucleate and grow the Kirkendall voids. In this kinetic mode, Cu diffusion is assumed.

The nucleation of a Kirkendall void requires super-saturation of vacancies, which can be affected by the density of vacancy sinks in the Cu. It is known in industry that when cool-rolled Cu is used as UBM, much less Kirekndall voids were found. This is also true in using nano-twinned Cu as UBM. On the other hand, when electroplated and large-grained Cu is used, much more Kirkendall voids are observed. When there is a large number of Kirkendall void at the Cu_3Sn/Cu interface, it will reduce the effective area of interdiffusion and in turn it will affect the reaction as well as the lattice shift discussed in the previous section.

4.6 Crystal Structure and Lamellar Structure of Cu_3Sn

The crystal structure of Cu_3Sn is orthorhombic. The powder diffraction pattern of Cu_3Sn is given in JCPDS Card No. 65-4653. The crystal of Cu_3Sn has been shown to form super-

lattices with a hexagonal symmetry. The hexagonal plane is a low energy plane. Since the porous Cu_3Sn has a very large area of free surfaces, we expect the lamellar surface to have low surface energy. It is possible that the lamellae could form on the (002), (020) and (200) planes in Cu_3Sn and also on the super-lattice plane. A detailed x-ray diffraction, TEM, and EBSD study of the lamellar structure will be needed in order to confirm its surface orientation and structure.

4.7 Conclusions

The formation processes of experimentally observed layer-type and porous-type Cu_3Snhave been interpreted in terms of chemical reactions in Cu-Sn microbumps. In the layer type formation, Cu is the dominant diffusing species and it reacts with Cu_6Sn_5 to form the layer-type Cu_3Sn. The vacancy flux needed for the Cu diffusion can lead to Kirkendall void formation, but no porous structure formed. The kinetics of growth of the layer-type Cu_3Sn assumes lattice shift. In the porous-type Cu_3Sn formation, Sn is the dominant diffusing species. The Sn is depleted from Cu_6Sn_5 and is driven to the side wall of Cu column in the microbump to form Cu_3Sn. The vacant sites left behind by the outer-diffusion of Sn are not absorbed by the Cu_3Sn lattice, and they join to form lamellar voids. There is no lattice shift. The volume fraction of voids is nearly 40%. The necessary and sufficient conditions of porous Cu_3Sn formation are postulated.

Chapter 5 A Comparative Study of Incomplete and Complete Cellular Precipitations

The formation of porous Cu_3Sn discussed in Chapters 2 to 4 is a complete cellular precipitation. This is rare and unique situation in phase transformations because classical cellular precipitation is an incomplete reaction, in which not all the supersaturated solutes can be precipitated out [42-47]. In 2014, Panchenko *et al*. reported the porous Cu_3Sn formation in microbumps for 3DIC packaging technology and identified it to a complete cellular precipitation [24]. Similar observations were subsequently made by the UCLA/NCTU team [25-28]. Gusak, Chen, and Tu developed a kinetic model, which explains the phenomenon as flux-driven cellular precipitation in an open system [41].

Recently, Tu and Gusak made a detailed comparison between the kinetics of complete and incomplete precipitations for a deeper understanding of their differences [48]. In this chapter, we will further understand the formation process of porous Cu_3Sn from the perspective of their comparative study. The detailed kinetic analysis of growth in Ref. [41] is not discussed here. However, some of its results are referenced.

5.1 Kinetics of Incomplete Cellular Precipitation

Following Refs. [44, 45, and 48], we first consider an example of classical incomplete cellular precipitation: the room temperature aging of Pb−7 at.%Sn alloy [42, 46]. It is modeled in Figure 5-1, in which a horizontal cell boundary of effective thickness δ is moving at velocity V along the vertical y-axis into the Pb(Sn) alloy. The transformed region behind the boundary has a periodic structure of two lamellae. Since lattice diffusion in the Pb(Sn) alloy can be ignored at room temperature, there is no lateral diffusion of Pb. So one of the lamellae (of width t) is the precipitate of the diffusing Sn along the cell boundary. The other lamella is the remaining Pb(Sn) alloy (of width S).

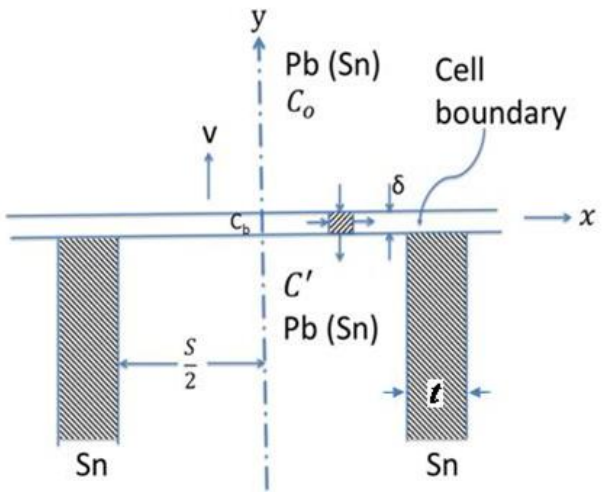

Figure 5-1 A schematic diagram of incomplete cellular precipitation. The cell boundary moves upward at velocity *V* into the untransformed Pb(Sn) alloy, leaving behind a periodic lamellar structure of Sn precipitate of width *t* and the remaining Pb(Sn) alloy of width *S* (adapted from Ref. [48]).

Let C_b, C', and C_0 be the Sn concentration in the cell boundary, the partially depleted Pb(Sn) alloy, and the parent Pb(Sn) alloy, respectively. Consider a small volume (the shaded area in Figure 5-1) within the cell boundary. In the 2-dimensional model, all concentrations are independent of *z* and, for simplicity, we assume that C_b varies only along *x*. Therefore, in the reference frame moving with the cell boundary, the divergence of the Sn flux (**J**) in the small volume is

$$\nabla \cdot \mathbf{J} = \frac{\partial}{\partial x}(-D_b \frac{\partial C_b}{\partial x}) + \frac{\Delta J_y}{\Delta y} \qquad (11)$$

where D_b is the diffusivity. The first term gives the rate of change of C_b due to unequal fluxes of Sn ($J_b = -D_b \partial C_b / \partial x$) diffusing across the right and left sides of the volume. Since the volume is moving upward (at velocity *V*), the parent alloy (of concentration C_0) enters into the

volume from the top side as an incoming flux ($J_{y1} = VC_0$). At the same time, an outgoing flux ($J_{y2} = VC'$) leaves the volume from the bottom side to precipitate on the cellular structure (of concentration C'). The difference ($\Delta J_y = J_{y2} - J_{y1}$) also contributes to the rate of change of C_b through the second term in Eq. (11). At the steady state, the net J_b and J_y fluxes into the volume is zero, so $\forall \cdot \mathbf{J} = 0$ and Eq. (11) gives the differential equation:

$$D_b \frac{\partial^2 C_b}{\partial x^2} + \frac{V}{\delta}(C_0 - C') = 0 \qquad (12)$$

where we have let $\Delta y = \delta$. In Eq. (12), the variables C_b and C' are related by

$$\frac{C'}{C_b} = k, \qquad (13)$$

where k is an assumed partition coefficient in the range $1 \geq k > C_e/C_0$ [45], Applying the boundary conditions: $dC_b/dx = 0$ at $x = 0$ and $C' = C_e$ at $x = S/2$, Cahn obtained the following solution for C' [44]:

$$\frac{C' - C_0}{C_e - C_0} = \frac{\cosh(\sqrt{\alpha} x / S)}{\cosh(\sqrt{\alpha}/2)} \qquad (14)$$

where

$$\alpha = \frac{kVS^2}{D_b \delta} \qquad (15)$$

In Eq. (14), k, V, S, D_b, and δ are all combined into one single parameter α. Also, C' and C_e can be normalized to C_0 (a constant). We may therefore plot C'/C_0 for a wide range of α to observe some general trend. In Figure 5-2, C'/C_0 is displayed as a function of x for $C_e/C_0 = 0.2$ and $\alpha = 0$, 3, 10, 100, and 1,000.

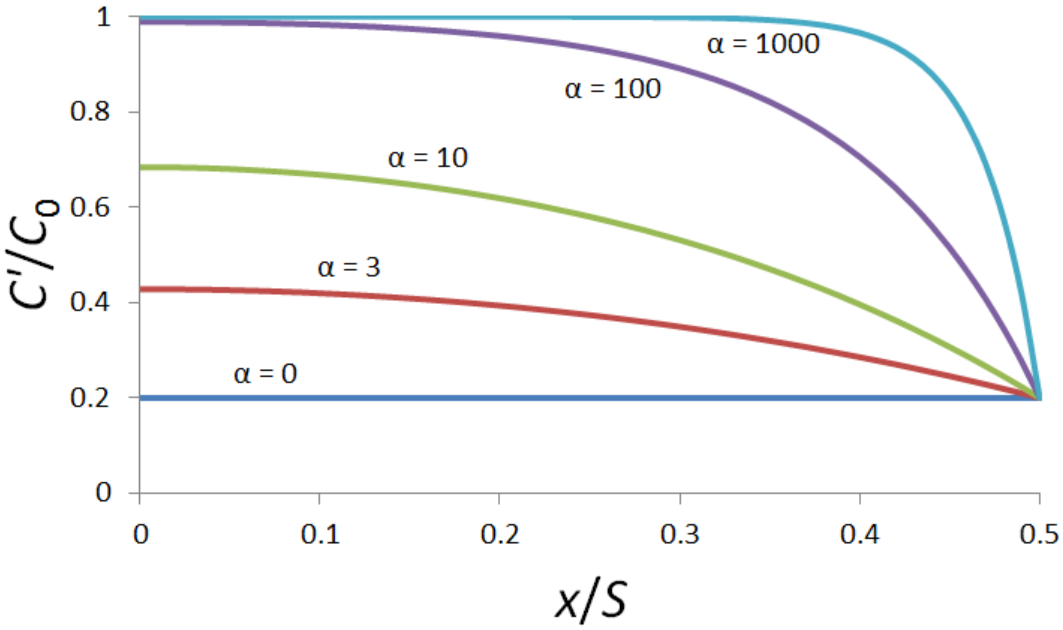

Figure 5-2 C'/C_0 as a function of x/S for C_e/C_0 = 0.2 and α = 0, 3, 10, 100, and 1,000.

It can be seen in Figure 5-2 that, for all non-zero α values, C'/C_0 varies along x. The reason is a gradient of concentration is required for the diffusion to take place unless there is unlimited time for diffusion (i.e. $\alpha = 0$ or $V = 0$). This is consistent with Cahn's statement that, if the diffusion is limited to the advancing cell boundary, the lamellae of cell cannot reach equilibrium composition at any non-zero growth rate [44].

The physical meaning for the parameter α in Eq. (15) is: A larger lamellar spacing (S), shorter diffusion time (δ/V), or smaller diffusivity (D_b) makes it more difficult to reach an equilibrium composition. All these factors contribute to a larger α. Hence, Figure 5-2 shows a greater departure of C' from the equilibrium value C_e (assumed to be $0.2C_0$ in Figure 5-2) at a larger α.

Another quantity of interest, defined as Q, is the fraction of the supersaturated solute that has been precipitated out. In the Pb(Sn) lamella, the fraction of Sn precipitated out of the

parent phase is $(C_0–C')/(C_0–C_e)$, where C' is a function of x and C_e is the equilibrium concentration. Thus, Q is given by an integration the numerator over the interlamellar spacing S, with the denominator multiplied by S [44, 45]:

$$Q = \frac{2\int_0^{\frac{S}{2}}(C_0 - C')dx}{(C_0 - C_e)S} = \frac{2}{\sqrt{\alpha}}\tanh\frac{\sqrt{\alpha}}{2}, \qquad (16)$$

where we have assumed $S>>t$, which also holds for Eq. (14). Two limiting cases of Eq. (16) are given in [45]:

$$\lim_{\alpha\to 0} Q = 1 \qquad (17a)$$

$$\lim_{\alpha\to\infty} Q = 0 \qquad (17b)$$

The $\alpha\to 0$ limit represents complete precipitation, while the $\alpha\to\infty$ limit represents complete suppression of precipitation. Both limiting cases are of theoretical interest, but unrealizable in practice. Here, we display Q graphically as a function of α between the 2 limits. As shown in Figure 5-3, Q has a value between 0 and 1, as is expected of incomplete precipitation. Its dependence on α matches the trend shown in Figure 5-2 very well.

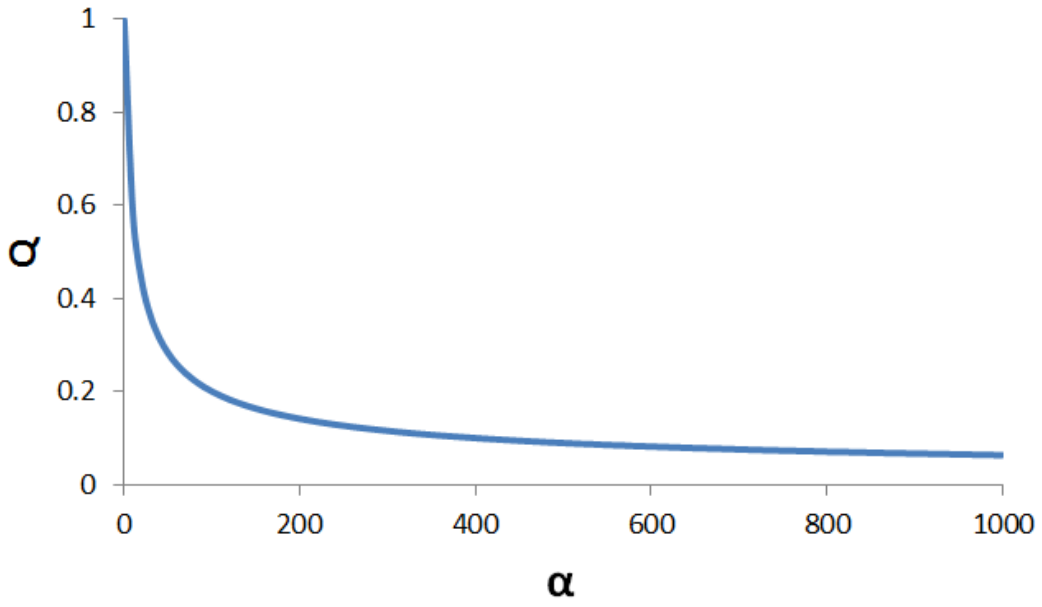

Figure 5-3 A graphic illustration of Q as a function of α.

5.2 Kinetics of Complete Cellular Precipitation

The experimentally-observed complete transformation of Cu_6Sn_5 to porous Cu_3Sn (e.g. Figures 3-2 and 3-3 in Ch. 3 and Figure 5-4 below) is due to a complete out-flux of Sn from the Cu_6Sn_5 phase. The transformation started from a Cu–Sn intermetallic compound in a layered structure of $Cu/Cu_3Sn/Cu_6Sn_5/Cu_3Sn/Cu$ [Figure 5-4(a)]. Then, the middle layer of Cu_6Sn_5 is gradually replaced by porous Cu_3Sn structure growing from periphery towards the center till the full disappearance of Cu_6Sn_5 [Figure 5-4(b)]. Significantly, the empty lattice sites left behind by the out-diffusion of Sn keep growing so that the porous structure is formed of two phases and one of them is a void (pores).

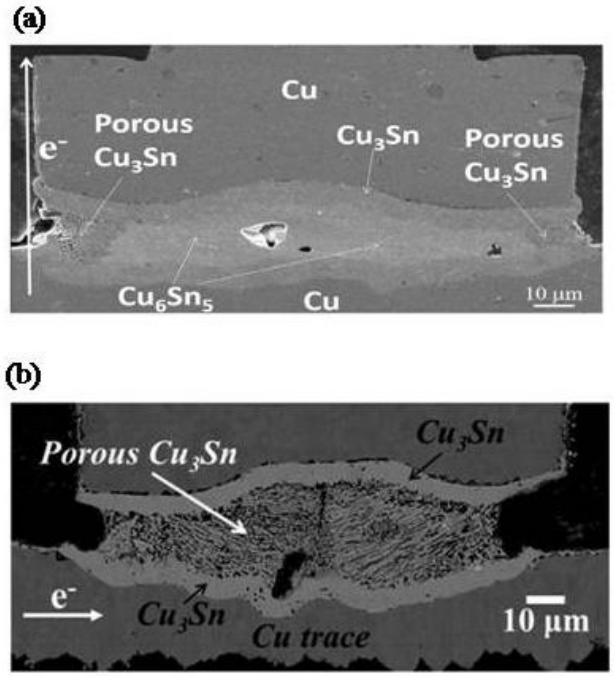

Figure 5-4 Cross-sectional view of (a) the starting stage and (b) final stage of Cu_3Sn porous structure formation (from Ref. [41]).

According to the experimental results, Gusak, Chen, and Tu developed a kinetic theory to explain the formation of porous Cu_3Sn with a lamellar structure, in which several possible

explanations are proposed and compared [41]. The most reasonable one is based on the flux-driven cellular precipitation in an open system. More recently, based on the sophisticated theory in [41], Tu and Gusak derived a simple formula for the prediction of the lamellar structure growth velocity [48], which agrees reasonable well with experimental data. They also made a comparison between the mechanisms of complete and incomplete precipitations, using the model depicted in Figure 5-5. Similar to the model in Figure 5-1, the cell boundary is moving into an unreacted region (Cu_6Sn_5) and a periodic lamellar structure forms behind the boundary. However, in contrast to the model in Figure 5-1, the lamellar structure consists of Cu_3Sn lamellae and "pores". The pores are left behind by the out-diffusing Sn.

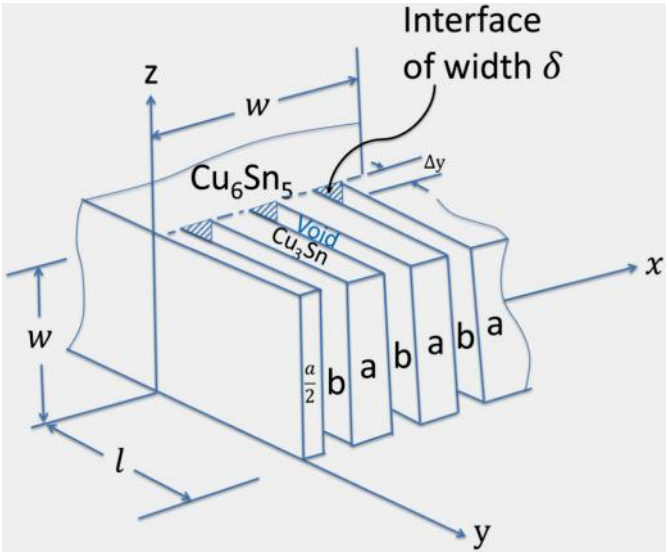

Figure 5-5 A schematic diagram of the growth of porous Cu_3Sn. The porous $Cu_3Sn$is a periodic lamellar structure formed of Cu_3Sn lamellae of width *a* and pores of width *b* (from Ref. [48]).

As discussed in Chapter 4, isolated Cu_6Sn_5 is an equilibrium phase. In order to decompose Cu_6Sn_5 by the reaction: $Cu_6Sn_5 - 3Sn \rightarrow 2Cu_3Sn$, there must be a sink to attract Sn. Experimentally, it has been found that the side wall of Cu column serves as such a sink in which Sn reacts with Cu to form Cu_3Sn. On the other hand, the empty lattice sites left behind

by the outgoing Sn atoms grow to open-ended pores. The time for out-diffusion of Sn in the open channels is thus unlimited. This results in the complete transformation of Cu_6Sn_5 to porous Cu_3Sn, which in turn makes it possible to determine the kinetic parameters in the process. For example, the molar volume of Cu_6Sn_5 and Cu_3Sn are 118.72 cm^3 and 35.01 cm^3, respectively. In the reaction: $Cu_6Sn_5 - 3Sn \rightarrow 2Cu_3Sn$, the Sn atoms diffuse away. So one mole of Cu_6Sn_5 converts into two moles of Cu_3Sn. The voids left behind by the Sn atoms has a volume of $118.72 - 2 \times 35.01\ cm^3 = 48.7\ cm^3$. Thus, the fraction of voids in the porous Cu_3Sn is

$$\frac{b}{a+b} = \frac{48.7}{118.42} \approx 41\%, \tag{18}$$

where a and b are the width of the Cu_3Sn lamellae and pores, respectively (Figure 5-5).

Form the theoretical volume ratio of voids in Eq. (18), the growth rate of porous Cu_3Sn can be determined by the law of conservation of mass as in [48]. Consider an interface (cell boundary) of area W^2 and thickness δ as shown in Figure 5-5. Assume that, in a time interval Δt, the interface moves a distance of Δy into the unreacted Cu_6Sn_5. So, a volume of $W^2\Delta y$ of Cu_6Sn_5 has been transformed into the porous Cu_3Sn. Using the theoretical volume of voids in the porous structure in Eq. (18), we obtain the total number of Sn atoms depleted from Cu_6Sn_5:

$$\#\mathrm{Sn} = \frac{0.41W^2\Delta y}{\Omega} \tag{19}$$

where Ω is the atomic volume of Sn.

Then we consider the flux of Sn atoms (J_b) diffusing out of Cu_6Sn_5 in the x-direction on the interface. Let C_b and M be the concentration and mobility of the Sn atoms, respectively. The driving force (F) is the gradient of the chemical potential (μ) of a Sn atom. Therefore, J_b can be written

$$J_b = C_b M\left(-\frac{\Delta\mu}{\Delta x}\right) = C_b \frac{D_b}{kT}\left(-\frac{\Delta\mu}{\Delta x}\right), \tag{20}$$

where M is related to the diffusivity (D_b) by $M = D_b/kT$ (Ref. [49], p. 65). In $(-\Delta\mu/\Delta x)$, the negative sign implies that F is in the direction of decreasing μ.

In Figure 5-5, total number of $(a+b)$ layers in the interface of width W is $n = W/(a+b)$. Each Cu_3Sn lamella has two surfaces with a height (in z) of W and thickness (in y) of δ. So the total cross-sectional area (A) for out-diffusion of Sn along x is

$$A = 2nW\delta = \frac{2W^2\delta}{a+b} \tag{21}$$

From Eqs. (20) and (21), we obtain the total flux of Sn atoms diffused out from the depletion of Cu_6Sn_5 (in the time interval Δt):

$$\#\text{Sn} = J_b A\Delta t = C_b \frac{D_b}{kT}\left(-\frac{\Delta\mu}{\Delta x}\right)\frac{2W^2\delta}{a+b}\Delta t \tag{22}$$

By the law of conservation of mass, the right hand sides of Eqs. (19) and (22) must be equal. Thus, equating the two sides gives the growth rate (V) of porous Cu_3Sn:

$$V = \frac{\Delta y}{\Delta t} = \frac{\Omega}{0.41} C_b \frac{D_b}{kT}\left(-\frac{\Delta\mu}{\Delta x}\right)\frac{2\delta}{a+b} \tag{23}$$

In Eq. (23), we may let $\Delta\mu = \Delta\mu^{\text{along } x}$ for the reason that the dominant chemical decomposition (hence the major chemical potential drop) occurs in the interface. In the rigorous treatment by Gusak, Chen, and Tu [41], Δx along the interface is divided into two parts: the Cu_6Sn_5/Cu_3Sn interface and the Cu_6Sn_5/void interface. By solving the diffusion equations in each part, the widths of the two parts (a and b) can be quantitatively determined [41]. Here, for simplicity, we let $\Delta x = (a+b)/2$. Equation (23) then becomes

$$V = \frac{\Omega}{0.41} C_b D_b \frac{\Delta\mu^{\text{along } x}}{kT}\frac{4\delta}{(a+b)^2} \tag{24}$$

As a numerical example, a unit cell of the Sn lattice has a volume of 109×10^{-24} cm^3 and 4 atoms per cell. So the atomic volume of Sn is $\Omega = 27.2 \times 10^{-24}$ cm^3. The formation energy

per atom of Cu_3Sn from the Cu/Cu_6Sn_5 reaction is $\Delta g \approx 0.75 \times 10^{-20}$ J, and $\Delta g/kT \approx 1$ at T = 523 K [41]. So we take $\Delta\mu^{\text{along x}}/kT \approx 1$ at T = 492 K. For the other parameters, we let $C_b \approx (5/11) \times 10^{22}$ atoms/cm^3, $D_b \approx 10^{-7}$ cm^2/s. a = 1.3 μm and b = 0.43 μm (as calculated in [41]), and $\delta \approx 3\times10^{-8}$ cm, where δ is the diameter of a Sn atom. Equation (24) then gives

$$V \approx \frac{27.2\times10^{-24}\ \text{cm}^3}{0.41}\left(\frac{5}{11}\times10^{22}\ \text{cm}^{-3}\right)\left(10^{-7}\ \frac{\text{cm}^2}{s}\right)\times1\times\frac{4\times3\times10^{-8}\ \text{cm}}{1.73\times10^{-4}\ \text{cm}^2}$$
$$\approx 1.2\times10^{-8}\ \text{cm/s} \qquad (25)$$

By comparison, the more rigorous approach in [41] gives $V \approx 10^{-7}$ cm/s and, experimentally, $V \approx 5 \times 10^{-9}$ cm/s.

5.3 Comparison between Incomplete and Complete Cellular Precipitations

Figures 5-6(a) and (b) illustrate the incomplete cellular precipitation of Pb(Sn) (Sec. 5.1) and the complete cellular precipitation of porous Cu_3Sn (Sec. 5.2).

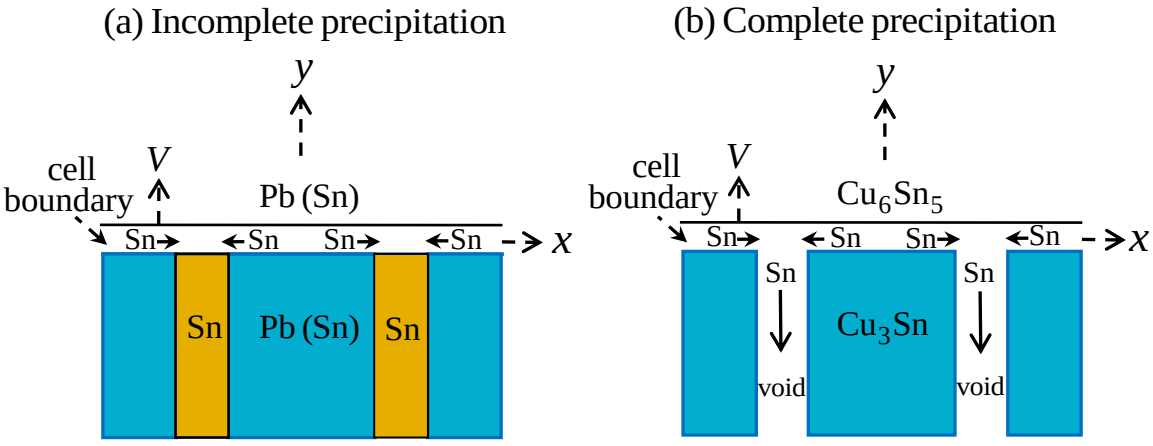

Figure 5-6 Schematic diagrams of (a) the incomplete cellular precipitation and (b) the complete cellular precipitation.

Based on these schematic diagrams, a comparison can be made between these two types of cellular precipitations.

(1) Similarities

1. Both have a cell boundary moving into the parent phase. The boundary is a reaction front, in which phase decomposition takes place.

2. In both cases, the end product is a lamellar structure composed of two phases.

(2) Differences

However, there are also significant differences:

1. In the Pb(Sn) case, both lamellae are solid solutions. In the Pb(Sn) case, one of the lamellae is a void.

2. In the Pb(Sn) case, the lamellar structure consists of the parent phase partially depleted of solute Sn and a precipitate that acts as a sink for the rejected Sn. In the porous Cu_3Sn case, one of the lamellae is an IMC (Cu_3Sn) different from the parent IMC (Cu_6Sn_5).

3. In the Pb(Sn) case, there is no lateral diffusion of Pb. In the porous Cu_3Sn case, since the phase changes from Cu_6Sn_5 to Cu_3Sn, interdiffusion of Sn and Cu along the interface must be considered [41].

(3) Consequences of the Differences

The consequences of these differences are substantial, as discussed below:

1. In the Pb(Sn) case, Sn diffusion is limited within the cell boundary between two solid solutions [Figure 5-6(a)]. Therefore, the lamellae cannot reach equilibrium composition at any non-zero growth rate, as shown analytically in Eq. (14) and quantitatively in Figure 5-2. So, we have the case of incomplete precipitation in a closed system. On the other hand, in the Cu_3Sn case, Sn atoms diffuse not only horizontally in the cell boundary, but also vertically in

empty channels with open ends [Figure 5-6(b)]. The empty and open-ended vertical channels allow unlimited diffusion time, which is a case of complete precipitation in an open system.

2. For incomplete precipitation, the kinetic parameters cannot be defined. They are combined into a single parameter [α in Eqs. (14)-(16)]. For example, in Eq. (16), V and S cannot be independently determined even if Q can be measured experimentally. However, in the case of complete precipitation, the end products are in equilibrium composition. Consequently, all the kinetic parameters can be unambiguously defined and determined, as has been shown in Ref. [41].

5.4 Conclusions

A comparison with the classical incomplete precipitation in terms of the lamellar structure composition, Sn diffusing channel, and kinetic parameter determination has led to a clearer physical picture of the formation mechanism of porous Cu_3Sn IMC in microbumps for 3D-IC packaging.

Chapter 6 Summary

Microbumps are widely used to interconnect stacked chips with through-Si-vias (TSVs) in vertical direction to enable 3D IC integration. Most of the microbump materials constituents are composed of Cu-Sn intermetallic compounds. Recent studies reported the formation of porous Cu_3Sn in Cu-Sn microbumps [24, 25], which is unseen in traditional flip-chip solder joints. Motivated by this discovery and its potential significance as a new failure mechanism in 3D IC packaging, we have conducted an experimental study on the formation processes of porous Cu_3Sn IMC in microbumps and a theoretical investigation in the formation mechanisms.

In the first set of experiments (Chapter 2), SnAg solder bump samples with Cu UBM were stressed at current densities of 1.45×10^4 A/cm^2 and 1.20×10^4 A/cm^2 and operating temperatures of approximately 185 ^oC and 170 ^oC, respectively. A porous Cu_3Sn structure was observed in the process. Cu_3Sn IMCs were also observed on the side walls of Cu column UBM due to side wall reactions. Previously, the layer-type Cu_3Sn is regarded as the terminal phase for the solid-state Cu-Sn reactions; however, our results conclude that the SnAg bump with low bump height would lead to porous-type Cu_3Sn formation when it is stressed with high current densities and high temperatures.

The second set of experiments (Chapter 3) put emphasis on the growth competition between the porous-type and layer-type of Cu_3Sn in solder microbumps. In the latter, we assume that Cu is the dominant diffusing species and it reacts with Cu_6Sn_5 to grow the layer-type Cu_3Sn. In the former, we assume that Sn is the dominant diffusing species. The Sn is depleted from Cu_6Sn_5 and is driven to the side-wall of Cu column in the microbump to form a coating of Cu_3Sn. The depleted Cu_6Sn_5 transforms to porous Cu_3Sn. The growth competition has been analyzed.

Experimental observations of 3-dimensional volumetric distribution of porous voids in Cu_3Sn-based microbumps by synchrotron X-ray tomography are presented. A 2-dimensional cross-sectional tomography view of the porous structure with SEM images is also given. The comparison of 3D and 2D identification of porous void distribution (~40%) is found to be consistent.

The formation processes of experimentally observed layer-type and porous-type Cu_3Sn have been interpreted in terms of chemical reactions in Cu-Sn microbumps (Chapter 4). In the layer type formation, Cu is the dominant diffusing species and it reacts with Cu_6Sn_5 to form the layer-type Cu_3Sn. The vacancy flux needed for the Cu diffusion can lead to Kirkendall void formation, but no porous structure formed. The kinetics of growth of the layer-type Cu_3Sn assumes lattice shift. In the porous-type Cu_3Sn formation, Sn is the dominant diffusing species. The Sn is depleted from Cu_6Sn_5 and is driven to the side wall of Cu column in the microbump to form Cu_3Sn. The vacant sites left behind by the outer-diffusion of Sn are not absorbed by the Cu_3Sn lattice, and they join to form lamellar voids. There is no lattice shift. The volume fraction of voids is nearly 40%. The necessary and sufficient conditions of porous Cu_3Sn formation are postulated.

Finally, in Chapter 5, a comparative study of complete and incomplete precipitations in terms of lamellar structure composition, Sn diffusing channel, and kinetic parameter determination has led to a clearer physical picture of main subject in early chapters: formation mechanism of porous Cu_3Sn IMC in microbumps for 3D-IC packaging.

References

[1] K. N. Tu, Reliability Challenges in 3D IC Packaging Technology. Microelectronics Reliability 51.3, 517-523 (2011).

[2] K. N. Tu, Solder Joint Technology. Springer: New York, NY (2007).

[3] L. F. Miller, Controlled collapse reflow chip joining. IBM J. Res. Dev. 13, 239-250 (1969).

[4] P. A. Totta and R. P. Sopher, SLT device metallurgy and its monolithic extensions. IBM J. Res. Dev. 13, 286-296 (1969).

[5] K. Puttlitz and P. Totta, Area array technology handbook for microelectronic packaging. Kluwer Academic, Norwell, MA (2001).

[6] International Technology Roadmap for Semiconductors. Semiconductor Industry Association, San Jose, CA (1999). See website http://public.itrs.net/

[7] K. N. Tu, H. Y. Hsiao, and C. Chen, Transition from flip chip solder joint to 3D IC microbump: Its effect on microstructure anisotropy. Microelectronics Reliability53, 2-6 (2013).

[8] Y. Li and D. Goyal (editors), 3D Microelectronic Packaging: From Fundamentals to Applications. Springer: New York, NY (2017).

[9] J. C. Lin, W. C. Chiou, K. F. Yang, H. B. Chang, Y. C. Lin, E. B. Liao, J. P. Hung, Y. L. Lin, P. H. Tsai, Y. C. Shih, T. J. Wu, W. J. Wu, F. W. Tsai, Y. H. Huang, T. Y. Wang, C. L. Yu, C. H. Chang, M. F. Chen, S. Y. Hou, C. H. Tung, S. O. Jeng, and D. C. H. Yu, High density 3D integration using CMOS foundry technologies for 28 nm node and beyond, in IEEE International Electron Device Meeting (2010), pp. 2.1.1–2.1.4.

[10] A. Yu, J. H. Lau, S. W. Ho, A. Kumar, W. Y. Hnin, D. Q. Yu, M. C. Jong, V. Kripesh, D. Pinjala, and D. L. Kwong, Study of 15 μm pitch solder microbumps for 3D IC integration, inElectronic Components and Technology Conference (ECTC) (2009), pp. 6–10.

[11] Y. Wang, Y. Liu, M. Li, K. N. Tu, and L. Xu, Interconnect quality and reliability of 3D packaging, in 3D Microelectronic Packaging (pp. 375-420), Springer International Publishing (2017).

[12] K. N. Tu, Electronic Thin-Film Reliability. Cambridge University Press (2010).

[13] K. N. Tu, Recent advances on electromigration in very-large-scale-integration of interconnects. J. Appl. Phys. 94, 5451–5473 (2003).

[14] C. Chen, H. M. Tong, and K. N. Tu, Electromigration and Thermomigration in Pb-Free Flip-Chip Solder Joints. Rev. Mater. Sci., 40, 531–555 (2010).

[15] L. Xu, J. Han, J. J. Liang, K. N. Tu, and Y. Lai, Electromigration induced high fraction of compound formation in SnAgCu flip chip solder joints with copper column. Appl. Phys. Lett. 92, 262104 (2008).

[16] Y. C. Liang, C; Chen, and K. N. Tu, Sidewall wetting induced void formation due to small solder volume in microbumps of Ni/SnAg/Ni upon reflow. ECS Solid State Lett. 1, 60–62 (2012).

[17] C. Chen and S. W. Liang, Electromigration issues in lead-free solder joints. J. Mater. Sci. Mater. Electron. 18, 259–268 (2007).

[18] M. H. Chu, S. W. Liang, C. Chen, and A. T. Huang, Electromigration failure mechanism in Sn-Cu solder alloys with OSP Cu surface finish. J. Electron. Mater. 41, 2502–2507 (2012).

[19] K. Zeng and K. N. Tu, Six cases of reliability study of Pb-free solder joints in electronic packaging technology. Mater. Sci. Eng. R Rep. 38, 55–105 (2002).

[20] S. H. Chiu and C. Chen, Investigation of void nucleation and propagation during electromigration of flip-chip solder joints using x-ray microscopy. Appl. Phys. Lett. 262106 (2006).

[21] C. Y. Liu, C. Chen, C. N. Liao, and K. N. Tu, Microstructure-electromigration correlation in a thin stripe of eutectic SnPb solder stressed between Cu electrodes. Appl. Phys. Lett. 75, 58–60 (1999).

[22] S. W. Liang, Y. W. Chang, T. L. Shao, C. Chen, and K. N. Tu, Effect of three-dimensional current and temperature distributions on void formation and propagation in flip-chip solder joints during electromigration. Appl. Phys. Lett. 89, 022117 (2006).

[23] S. W. Liang, S. H. Chiu, and C. Chen, Effect of Al-trace degradation on Joule heating during electromigration in flip-chip solder joints. Appl. Phys. Lett. 90, 082103 (2007).

[24] I. Panchenko, K. Croes, I. De Wolf, J. De Messemaeker, E. Beyne, and K. J. Wolter, Degradation of Cu_6Sn_5intermetallic compound by pore formation in solid–liquid interdiffusion Cu/Sn microbump interconnects. Microelectr. Eng. 117, 26-34 (2014).

[25] C. Chen, D. Yu, and K. N. Chen, "Vertical interconnects of microbumps in 3D integration", MRS Bull. 40, 257-262 (2015).

[26] J. A. Lin, C. K. Lin, C. M. Liu, Y. S. Huang, C. Chen, D. T. Chu, and K. N. Tu, Formation mechanism of porous Cu_3Sn intermetallic compounds by high current stressing at high temperatures in low-bump-height solder joints. Crystals 6, 12 (2016).

[27] Y. Wang, D. T. Chu, and K. N. Tu, Porous Cu_3Sn formation in Cu-Sn IMC-based micro-joints. IEEE ECTC Proceedings, pp. 439-446 (2016).

[28] D. T. Chu, Y.C. Chu, J. A. Lin, Y. T. Chen, C. C. Wang, Y. F. Song, C. C. Chiang, C. Chen, and K. N. Tu, Growth competition between layer-type and porous-type Cu_3Sn in microbumps. Microelectron. Relia. 79, 32-37 (2017).

[29] L. Hoglund and J. Agren, Analysis of the Kirkendall effect, marker migration and pore formation. Acta Mat. 49, 1311-1317 (2001).

[30] H. Strandlund and H. Larrson, Prediction of Kirkendall shift and porosity in binary and ternary diffusion couples. Acta Mat. 52, 4695-4703 (2004).

[31] K. Zeng, R. Stierman, T. C. Chiu, K. Edwards, K. Ano, and K. N. Tu, Kirkendall void formation in eutectic SnPb solder joints on bare Cu and its effectonjoint reliability. J. Appl. Phys. 97, 024508 (2005).

[32] W. Chao, B. D. Harteneck, J. A. Liddle, E. H. Anderson, and D. T. Attwood, Soft X-ray microscopy at a spatial resolution better than 15 nm. Nature 435, 1210-1214 (2005).

[33] G. C. Yin, M. T. Tang, Y.F. Song, F. R. Chen, K. S. Liang, F. W. Duewer, W. Yun, C. H. Ko, and H. P. D. Shieh, An energy-tunable transmission x-ray microscope for differential contrast imaging with near 60-nm resolution tomography. Appl. Phys. Lett.88**,** 241115 (2006).

[34] Y. F. Song, C. H. Chang, C. Y. Liu, S. H. Chang, U. S. Jeng, Y. H. Lai, D. G. Liu, S. C. Chung, K. L. Tsang, G. C. Yin, J. F. Lee, H. S. Sheu, M. T. Tang, C. S. Hwang, Y. K. Hwu, and K. S. Liang, X-ray beamline for structural studies at the NSRRC superconducting wavelength shifter. J. Synchrotron Rad. 14, 320-325 (2007).

[35] Joint Electron Device Engineering Council (JEDEC). Guideline for Characterizing Solder Bump Electromigration Under Constant Current and Temperature Stress; JEDEC Standard JEP154; JEDEC: Arlington, VA, USA, 2008.

[36] Y. Park, S. Kim, J. Park, J. Kim, H. Son, K. Han, J. Oh, N. Kim, and S. Yoo, Current Density Effects on theElectrical Reliability of Ultra Fine-Pitch Micro-Bump for TSV Integration. in Proceedings of the 2013 IEEE63rd Electronic Components and Technology Conference, Las Vegas, NV, USA, 28–31 May 2013.

[37] H. Y. Hsiao, C. Hu, M. Guo, C. Chen, and K. N. Tu, Inhibiting the consumption of Cu during multiple reflows of Pb-free solder on Cu. Scr. Mater. 65, 907–910 (2011).

[38] I. Kawakatsu, T. Osawa, H. Yamaguchi, On the growth of alloy layer between solid copper and liquid tin. Trans JIM 13, 436-443 (1972).

[39] P. T. Vianco, J. A. Rejent, P. Hlava, Solid-state intermetallic compound layer growth between copper and 95.5 Sn-3.9 Ag-0.6 Cu solder. J. Electr. Mater. 33, 991-1004 (2004).

[40] L. S. Darken, Diffusion, mobility and their interrelation through free energy in binary metallic systems. Trans. AIME 175, 184-201 (1948).

[41] A. M. Gusak, C. Chen, K. N. Tu, Flux-driven cellular precipitation in open system to form porous Cu_3Sn. Philos. Mag. 96 (13), 1318-1331 (2016).

[42] D. Turnbull, H. N. Treaftis, Kinetics of precipitation of tin from lead-tin solid solutions. Acta Metall. 3, 43-54 (1955).

[43] D. Turnbull, Theory of cellular precipitation. Acta Metall. 3, 55-63 (1955).

[44] J. W. Cahn, The kinetics of cellular segregation reactions. Acta Metall. 7, 18-28 (1959).

[45] K. N. Tu, D. Turnbull, Analysis of kinetics of boundary diffusion limited cellular precipitation. Scr. Metall. 1, 173-180 (1967).

[46] K. N. Tu, D. Turnbull, Morphology of cellular precipitation of tin from lead-tin bicrystals-II. Acta Metall. 15, 1317-1323 (1967).

[47] M. Hillert, On theories of growth during discontinuous precipitation. Metall. Mater Trans. A 3, 2729-2741 (1972).

[48] K. N. Tu and A. M. Gusak, A comparison between complete and incomplete cellular precipitations. Scr. Materialia 146, 133–135 (2018).

[49] K. N. Tu, Electronic Thin-Film Reliability. Cambridge University Press (2010).